AD-A098 703 UNITED TECHNOLOGIES RESEARCH CENTER EAST HARTFORD CONN F/G 20/4
ANALYSIS OF LAMINAR AND TURBULENT SYMMETRIC BLUNT TRAILING-EDGE--ETC(U)
APR 81 V N VATSA, M J WERLE, J M VERDON N00019-80-C-0057
UNCLASSIFIED UTRC/R81-914986-5 NL

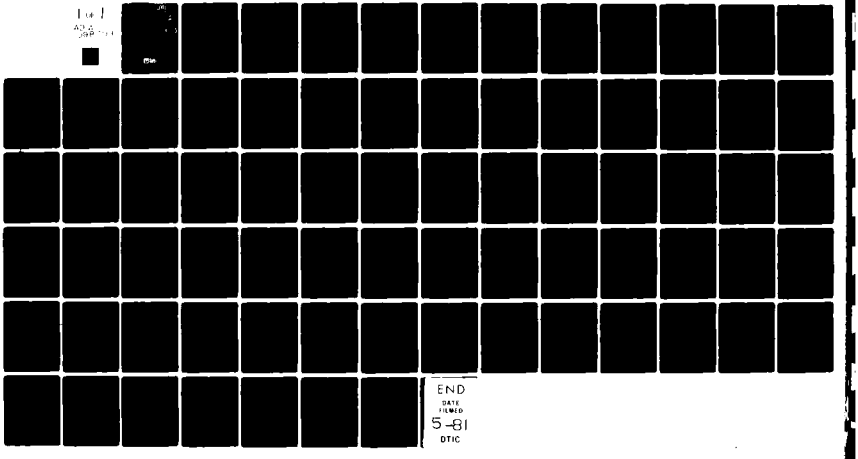

END
DATE FILMED
5-81
DTIC

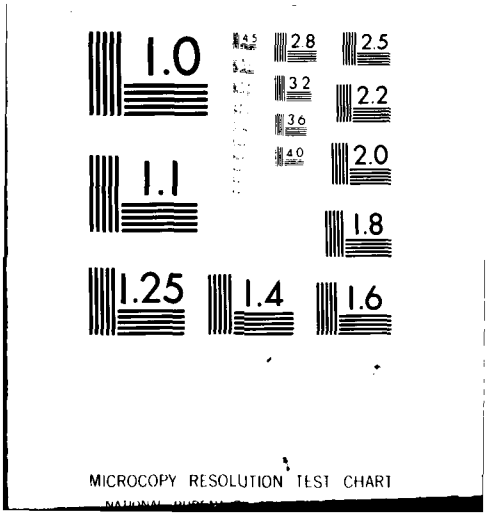
1.0
1.1
1.25
1.4
1.6
1.8
2.0
2.2
2.5
2.8
3.2
3.6
4.0
4.5
MICROCOPY RESOLUTION TEST CHART

R81-914986-5

LEVEL II

ANALYSIS OF LAMINAR AND TURBULENT SYMMETRIC BLUNT TRAILING-EDGE FLOWS

by

V.N. Vatsa, M.J. Werle and J.M. Verdon

April, 1981

Approved for Public Release; Distribution Unlimited

Final Report for Period 13 December 1979 — 13 January 1981

Prepared under Contract N00019-80-C-0057

for

Naval Air Systems Command
Department of the Navy
1499 Jefferson Davis Hwy.
Arlington, Va. 22209

by

UNITED TECHNOLOGIES RESEARCH CENTER
East Hartford, Connecticut 06108

UNCLASSIFIED (14) UTRC/R81-914986-5

SECURITY CLASSIFICATION OF THIS PAGE (When Data Entered)

REPORT DOCUMENTATION PAGE	READ INSTRUCTIONS BEFORE COMPLETING FORM
1. REPORT NUMBER: R81-914986-5 ✓	2. GOVT ACCESSION NO.: AD A098723 (9)
3. RECIPIENT'S CATALOG NUMBER	
4. TITLE (and Subtitle): Analysis of Laminar and Turbulent Symmetric Blunt Trailing-Edge Flows,	5. TYPE OF REPORT & PERIOD COVERED: Final Report, December 1979-Jan 1981 (13)
6. PERFORMING ORG. REPORT NUMBER: UTRC Report R81-914986-5	
7. AUTHOR(s): V. N. Vatsa, M. J. Werle, J. M. Verdon (10)	8. CONTRACT OR GRANT NUMBER(s): (15) N00019-80-C-0057
9. PERFORMING ORGANIZATION NAME AND ADDRESS: United Technologies Research Center, Silver Lane, East Hartford, CT 06108	10. PROGRAM ELEMENT, PROJECT, TASK AREA & WORK UNIT NUMBERS
11. CONTROLLING OFFICE NAME AND ADDRESS: (12) 75	12. REPORT DATE: Apr 1981 (11)
	13. NUMBER OF PAGES
14. MONITORING AGENCY NAME & ADDRESS (if different from Controlling Office): Department of the Navy, Naval Air Systems Command, 1499 Jefferson Davis Hwy, Arlington, VA 22209	15. SECURITY CLASS. (of this report): Unclassified
	15a. DECLASSIFICATION/DOWNGRADING SCHEDULE

16. DISTRIBUTION STATEMENT (of this Report)

Approved for Public Release; distribution unlimited

17. DISTRIBUTION STATEMENT (of the abstract entered in Block 20, if different from Report)

18. SUPPLEMENTARY NOTES

19. KEY WORDS (Continue on reverse side if necessary and identify by block number)

Interacting Viscous Flow, Finite Reynolds Number, Potential Inviscid Flow, Boundary Layer Equations, Viscous/Inviscid Iteration, Inverse Viscous Solution, Turbulent, Separated Flow, Symmetric, Blunt Trailing Edge.

20. ABSTRACT (Continue on reverse side if necessary and identify by block number)

Contributions are made to interacting viscous flow theory for symmetric separated flow past blunt airfoil trailing edges. A theoretical and computational technique for predicting turbulent, high Reynolds number, separation and near wake flow is provided. A detailed assessment of a viscous/inviscid iteration and an inverse boundary layer solution procedure is provided through a systematic series of test examples. These involve subsonic laminar and turbulent flows past flat plate and thickened flat plate (blunt trailing-

DD FORM 1 JAN 73 1473 EDITION OF 1 NOV 65 IS OBSOLETE
S/N 0102-LF-014-6601

UNCLASSIFIED
SECURITY CLASSIFICATION OF THIS PAGE (When Data Entered)

409252

cont

edged) airfoils. In addition, a general approach is outlined for incorporating local strong interaction solutions into an overall viscous solution procedure for isolated airfoils and cascades.

R81-914986-5

Analysis of Laminar and Turbulent Symmetric Blunt Trailing-Edge Flows

TABLE OF CONTENTS

R81-914986-5

Analysis of Laminar and Turbulent Symmetric Blunt Trailing-Edge Flows

SUMMARY

Contributions are made to interacting viscous flow theory for symmetric separated flow past blunt airfoil trailing edges. A theoretical and computational technique for predicting turbulent, high Reynolds number, separation and near wake flow is provided. A detailed assessment of a viscous/inviscid iteration and an inverse boundary layer solution procedure is provided through a systematic series of test examples. These involve subsonic laminar and turbulent flows past flat-plate and thickened flat-plate (blunt trailing-edged) airfoils. In addition, a general approach is outlined for incorporating local strong-interaction solutions into an overall viscous solution procedure for isolated airfoils and cascades.

INTRODUCTION

An important problem faced by the designer of advanced gas turbine engines is the prediction of high Reynolds number viscous flow and, in particular, viscous separation phenomena, in compressor and turbine blade passages. Viscous effects control exit flow angles, aerodynamic losses, heat transfer rates, and blade stall, and hence, must be accounted for. Clearly then, an analytical procedure for predicting viscous flow in high-performance compressor and turbine blade rows would be a significant contribution to the successful design process.

The overall goal of the present research program is to employ interacting viscous/inviscid flow concepts to develop a reliable analytical/numerical method for predicting viscous effects in subsonic to low supersonic cascade flows at high Reynolds numbers. The approach to be followed is similar to that being successfully applied to high Reynolds number external aerodynamic flows wherein viscous/inviscid interaction concepts are used to construct the full flow field with locally relevant component flow solvers (Ref. 1). Thus, for the case of high Reynolds number flow in a cascade, the full flow field is broken down into the four major categories to represent 1) the inviscid flow; 2) attached boundary layer flow; 3) wake flow; and 4) locally interacting (possibly separated) flow such as occurs at a blunt trailing edge. Construction of a general cascade flow solver involves first, the development of component flow solvers, and second, the matching of these component solvers into an overall computational procedure to produce a reliable and efficient general flow solver. Therefore, the utility and reliability of this cascade solver is critically dependent on the level of development of its component members. The first three components which deal with the inviscid flow, the boundary layer flow, and the wake flow are well understood fluid dynamically and solution methods are at a relatively mature state. Work on the fourth component, the local interaction solver, has been progressing at UTRC under contract with the Naval Air Systems Command. In the present phase of this effort, solution techniques have been developed and demonstrated for symmetric, blunt, trailing-edge flows.

The present effort is a continuation of the work initiated by Werle and Verdon (Refs. 2 through 5), in which a theoretical basis for addressing separated trailing-edge flows was established using asymptotic triple-deck concepts. A computational method for solving the triple-deck equations was first demonstrated for supersonic flow (Refs. 2 and 3) and then extended to subsonic flow (Refs. 4 and 5) using Carter's (Ref. 6) iterative technique. Thereafter, the theoretical concepts were generalized to the finite Reynolds number regime through introduction of a special separated flow coordinate system (Refs. 4 and 5). Turbulence effects were accommodated through introduction

of a turbulent version of the Levy-Lees transformation (Ref. 4). The goal of the current effort has been principally to refine, demonstrate and verify the theoretical and computational methods through application to symmetric high-Reynolds-number viscous flows past blunt airfoil trailing edges. In addition, attention has been given to comprehending the "local" viscous/inviscid interaction solver into a general aerodynamic formulation in which the local strong viscous/inviscid interaction solution is coupled to a global inviscid solution for cascade flow fields.

Results are presented here for a wide range of trailing edge flows. First, the basic finite difference algorithm is critically assessed through comparison with independent triple-deck solutions for laminar flat-plate trailing edge flow. Second, the interacting boundary-layer concept and solution algorithm is verified through a systematic Reynolds number study showing the necessary approach to the sharp and blunt trailing-edge, triple-deck, solutions as $Re \to \infty$. Third, the extension of the approach to turbulent trailing edge flows is verified by comparison with flat-plate experimental data; and finally, the solution procedure is demonstrated for symmetric, turbulent, blunt trailing-edge flows.

FINITE REYNOLDS NUMBER INTERACTION MODEL

General Concepts

For flows of practical interest in either external or internal aerodynamics the Reynolds number is usually sufficiently high so that the flow past an airfoil or blade can be divided into two regions: an "inner" dissipative region consisting of the boundary layer and the wake, and an "outer" inviscid region. The principal interaction between the viscous and inviscid regions arises from the displacement thickness effect leading to a thickened semi-infinite equivalent body and causing changes in surface pressures. If the interaction is "weak", the viscous effect on the pressure is small (i.e., of $O(Re^{-1/2})$ in laminar flow or of $O(\ln Re)^{-1}$ in turbulent flow (Ref. 7)), and the complete flow problem can be solved in a hierarchial manner (Ref. 8). The first step is to determine the inviscid flow past the airfoil. The resulting pressure distribution is then imposed on the viscous layer calculation to determine the displacement due to viscous dissipation and hence, the effective shape of the body. The displacement effect on the inviscid flow is then calculated to provide an updated surface pressure distribution.

The foregoing method for calculating the interaction between the viscous and inviscid parts of the flow is based on a direct hierarchy between the viscous and inviscid regions which applies as long as the disturbances to the inviscid flow due to viscous displacement effects are small. However, the flow over an airfoil involves both a weak overall interaction arising from standard displacement effects and also from wake curvature effects, and local "strong" interactions arising, for example, from boundary layer separation, shock boundary layer interaction, or the rapid flow acceleration immediately aft of the trailing edge. In such situations, viscous displacements cause substantial changes in the local inviscid pressure field. The concept of an inner viscous region and an outer inviscid region still applies but the direct hierarchial structure of the flow breaks down. In a strong interaction region the hierarchy changes from direct (i.e., pressure determined by the inviscid flow) to inverse (pressure determined by the viscous layer) and this change must be accommodated in developing a complete solution (Ref. 8).

The ultimate goal of the present research program is to develop a numerical solution procedure for high Reynolds number cascade flow. Our intent is to employ an interacting boundary layer approach in which the flow in the inviscid region is potential and the viscous flow is governed by Prandtl's boundary layer equations. Numerical solutions of the full-potential boundary value problem for subsonic (Ref. 9) or transonic (Ref. 10) cascades and direct solutions (i.e., pressure prescribed) for the boundary layer equations (Ref. 11) have been developed to a relatively mature state, but efficient and accurate

solutions for local strong viscous/inviscid interaction regions are still under development. In the present study attention has been focused on the trailing-edge problem. Here, the strong interaction arises from the abrupt change in the slip condition that the boundary layer experiences at the termination of the airfoil surface. This leads to a singularity in the classical boundary layer solution and subsequent local breakdown of a weak-interaction solution procedure. An important feature of the present formulation is the use of a shear layer coordinate (see Ref. 4) which departs from the airfoil surface upstream of the trailing edge and "reattaches" on the wake centerline (Fig. 1). After making the usual thin viscous layer assumptions in directions along and normal to the shear layer coordinate and applying Prandtl's transposition theorem, the classical form of the boundary layer equations are retained. The present report deals only with the symmetric, blunt, trailing-edge problem. Future work will be aimed at the extension of present concepts and solution procedures to compressor and/or turbine blade trailing-edge flows, which are strongly asymmetric, and thus require a consideration of wake curvature effects. The analysis described herein has been developed with this general problem in mind.

We consider high Reynolds number ($Re = \rho_\infty^* u_\infty^* L^* / \mu_\infty^*$) flow, with negligible body forces, of a perfect gas with constant specific heats and Prandtl number past a two-dimensional, symmetric airfoil. For symmetric flows it is sufficient to determine a solution only in the upper half-plane of the flow field. In the following discussion flow variables and spatial coordinates have been made dimensionless. Lengths have been scaled with respect to the length of the airfoil (L^*), density, velocity, and viscosity with respect to their free-stream values (ρ_∞^*, u_∞^* and μ_∞^*, respectively), pressure with respect to twice the free-stream dynamic pressure ($\rho_\infty^* u_\infty^{*2}$), and temperature with respect to the square of the free-stream speed divided by the specific heat at constant pressure (u^{*2}/c_p^*). Here the superscript * denotes a dimensional quantity, and the subscript ∞ refers to conditions at infinity.

Inviscid Region

The inviscid flow is assumed to be isentropic and irrotational. The velocity potential, Φ, is governed by the equation

$$A^2 \nabla^2 \Phi = \nabla\Phi \cdot \nabla (\nabla\Phi)^2/2 \tag{1}$$

The speed of sound propagation, A, the fluid pressure, p, density, ρ, and temperature, T, are determined by Bernoulli's equation and the isentropic relations; i.e.,

$$(M_\infty A)^2 = (\gamma M_\infty^2 p)^{(\gamma-1)/\gamma} = \rho^{(\gamma-1)} = (\gamma-1) M_\infty^2 T = 1 - \frac{(\gamma-1)}{2} M_\infty^2 \left[(\nabla\Phi)^2 - 1\right] \tag{2}$$

where M is the Mach number and γ is the specific heat ratio. The inviscid flow is determined as a solution of Eqs. (1) and (2) subject to conditions of flow tangency at the displacement surface, $\mathcal{D}$; i.e.,

$$\nabla\Phi\cdot\vec{n} = 0 \tag{3}$$

where $\vec{n}$ denotes the unit outward normal vector, and uniform flow in the far field; i.e.,

$$\nabla\Phi \rightarrow \vec{e}_x \text{ as } \vec{R}\rightarrow\infty \tag{4}$$

where $\vec{e}_x$ is a unit vector directed downstream along the airfoil chord (i.e., the x-axis) and $\vec{R}$ is a position vector emanating from a point on the airfoil. The displacement surface is defined by the equation

$$\mathcal{D}(s,n) = n - \delta(s) + t(s) = 0 \tag{5}$$

where s denotes the shear layer coordinate, n, is the coordinate normal to the shear layer coordinate, $\delta(s)$ is the viscous displacement thickness, and $n = -t(s)$ defines the airfoil surface. The displacement thickness is measured from the airfoil surface or wake centerline in a direction normal to the s-coordinate curve as shown in figure 1.

Solutions for interacting flows are determined by an iterative procedure which requires successive solutions for the viscous and inviscid regions. If the maximum distance between the displacement and shear-layer coordinate surfaces, $|\delta(s) - t(s)|_{max}$, is small, updated inviscid predictions can be determined efficiently by employing a perturbation analysis (c.f. Ref. 12). For this purpose the velocity potential is expanded in an asymptotic series; i.e.,

$$\Phi = \Phi_0 + \epsilon\Phi_1 + \mathcal{O}(\epsilon^2) = \Phi_0 + \phi + \mathcal{O}(\epsilon^2) \tag{6}$$

where $\epsilon \sim \mathcal{O}(|\delta - t|_{max})$. In addition, Taylor series expansions; e.g.,

$$\nabla\Phi_0\big|_{\mathcal{D}} = \nabla\Phi_0\big|_{\mathcal{S}} + (\delta - t)\frac{\partial}{\partial n}(\nabla\Phi_0)\big|_{\mathcal{S}} + \mathcal{O}(\epsilon^2) \tag{7}$$

are applied to refer conditions at the displacement surface, $\mathcal{D}$, to the shear layer coordinate surface, $\mathcal{S}$. Equations governing the zeroth and first-order potentials are obtained by substituting the series expansions, Eqs. (6) and (7), into the governing inviscid equations, Eqs. (1) through (4), equating terms with like powers of ϵ, and neglecting terms of second and higher order in ϵ.

The zeroth order potential, Φ_0, is a solution of the full-potential equation (Eqs. (1) and (2) with Φ and A replaced by Φ_0 and A_0, respectively) subject to the condition of flow tangency at the shear layer coordinate surface; i.e.,

$$\nabla\Phi_0 \cdot \vec{n}\Big|_{\mathcal{S}} = 0 \tag{8}$$

and uniform conditions in the far field

$$\nabla\Phi_0 \to \vec{e}_x\,, \qquad \vec{R} \to \infty \tag{9}$$

The first-order potential is a solution of the linear, variable-coefficient, differential equation

$$A_0^2\nabla^2\phi = \left[\nabla\Phi_0\cdot\nabla + (\gamma-1)\nabla^2\Phi_0\right](\nabla\Phi_0\cdot\nabla\phi) + \nabla\left[(\nabla\Phi_0)^2/2\right]\cdot\nabla\phi \tag{10}$$

where the coefficients depend on the zeroth-order solution. First-order conditions on the shear layer coordinate surface and in the far field are given by

$$\begin{aligned}\nabla\phi\cdot\vec{n} &= (\nabla\Phi_0\cdot\vec{\tau})\frac{d}{ds}(\delta-t) - (\delta-t)\frac{\partial^2\Phi_0}{\partial n^2} \\ &= \rho_0^{-1}\frac{\partial}{\partial s}\left[\rho_0(\nabla\Phi_0\cdot\vec{\tau})(\delta-t)\right], \qquad \text{on } \mathcal{S}\end{aligned} \tag{11}$$

and

$$\nabla\phi = 0, \qquad \vec{R} \to \infty \tag{12}$$

where $\vec{\tau}$ is a unit vector tangent to $\mathcal{S}$ and directed downstream. The inviscid pressure at the displacement surface is given by

$$p\Big|_{\mathcal{D}} = \left[p_0 + \epsilon p_1 + (\delta-t)\frac{\partial p_0}{\partial n}\right]_{\mathcal{S}} + O(\epsilon^2) \tag{13}$$

where

$$p_0 = (\gamma M_\infty^2)^{-1} (M_\infty A_0)^{2\gamma/(\gamma-1)}$$
$$= (\gamma M_\infty^2)^{-1} \left\{ 1 - \frac{(\gamma-1)}{2} M_\infty^2 \left[(\nabla \Phi_0)^2 - 1 \right] \right\}^{\gamma/(\gamma-1)} \tag{14}$$

and

$$(\epsilon p_1 + (\delta - t) \frac{\partial p_0}{\partial n})_{\mathcal{S}} = -(M_\infty A_0)^{2/(\gamma-1)} \left[\nabla \Phi_0 \cdot \nabla \phi + (\delta - t) \frac{\partial}{\partial n} (\nabla \Phi_0)^2 / 2 \right] \Big|_{\mathcal{S}} \tag{15}$$

Thus the inviscid pressure at the displacement surface, $\mathcal{D}$, is determined in terms of information supplied at the shear-layer coordinate surface, $\mathcal{S}$.

Realistic turbomachinery flow configurations frequently consist of thick, highly-cambered blades and large flow deflections due to high blade loading. Thus the general inviscid model derived above will be required for compressor or turbine interaction analyses. Numerical solutions of the nonlinear, zeroth-order (Ref. 9) and the linear, first-order (Ref. 13) potential equations have already been developed for cascade applications. These solutions and their associated computer codes can be readily modified and extended for viscous/inviscid interaction studies. However, in the present effort our primary concern has been the application of an inverse viscous solution procedure and a viscous/inviscid iteration procedure for calculating the flow in local strong-interaction regions. For this purpose the inviscid model can be simplified further by restricting consideration to symmetric flow past a thin airfoil. In this case the zeroth-and first-order boundary value problems can both be approximated by the classical small-disturbance equations, and the inviscid pressure distribution at the displacement surface can be determined by a Cauchy integral evaluation; i.e.,

$$p_{\mathcal{D}}(s) = (p_0 + \epsilon p_1)_{\mathcal{S}}$$
$$= p_\infty - \frac{(1-M_\infty^2)^{1/2}}{\pi} \left[\int_{-\infty}^{\infty} \frac{h'(\zeta) + t'(\zeta)}{s-\zeta} \, d\zeta + \int_{-\infty}^{\infty} \frac{\delta'(\zeta) - t'(\zeta)}{s-\zeta} \, d\zeta \right] \tag{16}$$
$$= p_\infty - \frac{(1-M_\infty^2)^{1/2}}{\pi} \int_{-\infty}^{\infty} \frac{h'(\zeta) + \delta'(\zeta)}{s-\zeta} \, d\zeta$$

where h(s) is the distance from the airfoil chord to the airfoil surface in the direction normal to the shear-layer coordinate, and the prime denotes differentiation. Note that to within the first-order approximation

$$p_{\mathcal{D}}(s) = p_{\mathcal{D}}(x) = p_\infty - \frac{(1-M_\infty^2)^{1/2}}{\pi} \int_{-\infty}^{\infty} \frac{h'(\zeta)+\delta'(\zeta)}{x-\zeta}\, d\zeta \tag{17}$$

where the airfoil thickness, h, and viscous displacement thickness, δ, distributions are now measured normal to the airfoil chord line.

Viscous Layer

The flow in the inner or viscous region is assumed to be governed by Prandtl's boundary layer equations referred to the shear-layer coordinate direction. A detailed derivation of these equations can be found in Ref. 2. After applying Prandtl's transposition; i.e., introducing the scaled normal coordinate, $\tilde{n}$, and velocity component, $\tilde{v}$, where

$$\tilde{n} = Re^{1/2}(n+t)$$
$$\tilde{v} = Re^{1/2}\left(v+u\frac{dt}{ds}\right) \tag{18}$$

and u and v are the fluid velocity components in the s and n-directions, respectively, the governing equations become

continuity

$$\frac{\partial(\rho u)}{\partial s} + \frac{\partial(\rho\tilde{v})}{\partial\tilde{n}} = 0 \tag{19}$$

s-momentum

$$\rho\left[u\frac{\partial u}{\partial s} + \tilde{v}\frac{\partial u}{\partial\tilde{n}}\right] - \rho_e u_e \frac{\partial u_e}{\partial s} = \frac{\partial}{\partial\tilde{n}}\left(\mu_T\frac{\partial u}{\partial\tilde{n}}\right) \tag{20}$$

energy

$$\rho\left[u\frac{\partial H}{\partial s} + \tilde{v}\frac{\partial H}{\partial n}\right] = \frac{\partial}{\partial\tilde{n}}\left[\frac{\mu_T}{\sigma}\frac{\partial H}{\partial\tilde{n}} + (\mu_T - \hat{\mu}_T/\sigma)\,u\frac{\partial u}{\partial\tilde{n}}\right] \tag{21}$$

Here $H = T + u^2/2$ is the total enthalpy, the viscosity, μ, is assumed to be a function of temperature alone, σ is the Prandtl number, the subscript e denotes properties at the edge of the boundary layer, and the effective turbulent viscosity terms μ_T and $\hat{\mu}_T$ are defined by

$$\mu_T = \mu + \gamma_T e$$
$$\hat{\mu}_T = \mu + \sigma \gamma_T e/\sigma_T \tag{22}$$

where e is the turbulent eddy viscosity, σ_T is the turbulent Prandtl number, and γ_T is the longitudinal intermittency factor.

The foregoing equations are solved subject to the following boundary conditions:

Edge Conditions $(\tilde{n} \to \infty)$

$$u \to u_e, H \to H_e \tag{23}$$

Airfoil Surface Conditions $(\tilde{n} = 0, s \leq s_{TE})$

$$u = \tilde{v} = 0 \tag{24}$$

and either

$$H = H_W(s) \text{ or } \frac{\partial H}{\partial \tilde{n}} = Re^{-1/2} q_W(s) \tag{25}$$

where H_W and $q_W(s)$ are prescribed functions

Wake Centerline Conditions $(n = 0, s > s_{TE})$

$$\tilde{v} = \frac{\partial u}{\partial \tilde{n}} = \frac{\partial H}{\partial \tilde{n}} = 0 \tag{26}$$

Finally, the displacement thickness of the viscous layer is defined by the relation

$$\delta(s) = Re^{-1/2} \int_0^\infty \left(1 - \frac{\rho u}{\rho_e u_e}\right) d\tilde{n} \tag{27}$$

Turbulence Model

The turbulence model employed in the present study is similar to the Cebeci-Smith (Ref. 14) eddy viscosity formulation as modified for flat-plate near-wake flows by Cebeci et al. (Ref. 15). Thus for wall boundary layers the eddy viscosity formulation considers inner and outer turbulence layers with

$$e = e_i = 0.16\, D^2 Re^{1/2} \rho \tilde{n} \mu^{-1} \left| \frac{\partial u}{\partial \tilde{n}} \right|, \qquad \tilde{n} < \tilde{n}_1 \tag{28a}$$

$$e = e_o = 0.0168\, \rho u_e \mu^{-1} Re^{1/2} \int_0^\infty (1 - \frac{u}{u_e})\, d\tilde{n}, \qquad \tilde{n} > \tilde{n}_1 \tag{28b}$$

and the two forms being equal at $\tilde{n} = \tilde{n}_1$. Here

$$D = \left[1 - \exp(-\tilde{n}/a)\right] \tag{29a}$$

where the length scale, a, is given by

$$a = 26 \mu\, Re^{-1/2} \left[\rho (1 - 11.8\, p^+) u_\tau\right]^{-1} \tag{29b}$$

and the pressure gradient, p^+, and shear velocity, u_τ, are defined by

$$p^+ = \mu u_e \frac{du_e}{ds} \Big/ (\rho u_\tau^3 Re) \tag{29c}$$

$$u_\tau = Re^{-1/4} \left[\mu \frac{\partial u}{\partial \tilde{n}} \Big/ \rho\right]^{1/2}_{\tilde{n}=0} \tag{29d}$$

In the wake, the inner region is further subdivided into two parts.

For $0 < \tilde{n} < \tilde{n}_2$

$$e_w = 0.4\, Re^{-1/2} \rho u_{\tau_E} \mu^{-1} \tilde{n}_c \tag{30a}$$

where $\tilde{n}_c$ is the value of $\tilde{n}$ such that

$$u_{calc} = 1.1\, u_{\tau_E} \left[2.5 \ln(Re^{-1/2} \rho u_{\tau_E} \mu^{-1} \tilde{n}) + 5.2\right] \tag{30b}$$

where u_{calc} is the computed velocity profile in the wake and u_{τ_E} is the shear velocity at a cusped trailing edge or at some specified location upstream of the trailing edge for a blunt trailing edge. When $\tilde{n}_2 < \tilde{n} < \tilde{n}_1$, equation (28a) is applied with D = 1. To prevent e_w from exceeding e_o at large distances downstream of the trailing edge, once $e_o = e_w$ the eddy viscosity for larger values of s is taken to be constant across the wake.

The longitudinal intermittency factor, γ_T, is taken to be the same as that employed by Harris (Ref. 16); i.e.,

$$\gamma_T = 1 - \exp\left[-0.412(s - s_{ti})^2 / \lambda_T^2\right] \tag{31a}$$

where s_{ti} is the location of transition initiation, and the scale length of the transition process is given by

$$\lambda_T = s_{\gamma_T=0.75} - s_{\gamma_T=0.25} \tag{31b}$$

Viscid/Inviscid Iteration

The complete flow field is determined as a solution of the inviscid equations subject to the condition of flow tangency at the displacement surface, $\mathcal{D}$, and a solution of the boundary layer equations which approaches inviscid conditions on $\mathcal{D}$ at the outer edge of the viscous layer (i.e., $u \to u_e$ and $H \to H_e$ as $\tilde{n} \to \infty$). Since the displacement surface must be determined as part of the overall solution, an iterative solution procedure is required. It has been found that a semi-inverse calculation using underrelaxation provides a relatively efficient method for determining the flow in strong viscous/inviscid interaction regions (Ref. 6). In this approach the inviscid and viscous equations are solved for a prescribed nth displacement thickness distribution, $\delta^n(s)$, to determine the (n + 1)th inviscid pressure distribution, $p_{inv}^{n+1}(s)$, at the displacement surface and the (n + 1)th pressure distribution, $p_{visc}^{n+1}(s)$, in the viscous layer. The (n + 1)th estimate for the displacement thickness is then obtained by underrelaxation i.e.,

$$\delta^{n+1}(s) = \delta^n(s)\left[1 + \omega\left[p_{inv}^{n+1}(s) - p_{visc}^{n+1}(s)\right]\right] \tag{32}$$

where $\omega<1$ is the relaxation parameter. The process is continued until

$$\left\|\delta^{n+1}(s) - \delta^n(s)\right\| < \epsilon_\delta \tag{33}$$

where $||\quad||$ is a suitably chosen norm; e.g.,

$$\left\|\delta^{n+1}-\delta^{n}\right\| = \frac{1}{s_f - s_i}\int_{s_i}^{s_f}\left|\delta^{n+1}-\delta^{n}\right| ds \tag{34}$$

Here $s = s_i$ and $s = s_f$ define the upstream and downstream boundaries of the strong interaction solution domain.

The foregoing procedure consists of direct solutions of the inviscid equations and inverse solutions of the viscous layer equations (i.e., δ is prescribed to determine both the inviscid and viscous pressure fields). An important advantage in applying an inverse procedure to determine the viscous flow field is that the boundary layer equations can be solved through a separation point and into a region of reversed flow, whereas a direct (i.e., $dp/ds = u_e\, du_e/ds$ is prescribed to determine $\delta(s)$) boundary layer solution will break down at a separation point.

VISCOUS REGION SOLUTION PROCEDURE

In the present study emphasis has been placed on the development of a viscous/inviscid iteration procedure and an inverse viscous solution procedure for finite-Reynolds-number, compressible, trailing-edge flow. For this purpose consideration was restricted to adiabatic flow at unit Prandtl numbers ($\sigma=\sigma_T=1$) past a symmetric, thin, blunt-edged airfoil. The iteration procedure between the viscous and inviscid solutions was described in the previous section and the inverse viscous layer procedure is presented here. The general viscous layer equations are first expressed in "turbulent" Levy-Lees type variables and then after appropriate simplifications are introduced, the viscous solution procedure is described for the special case of adiabatic flow. The computer code being developed in conjunction with the present analysis has been structured such that extensions to general aerodynamic profiles and heat conducting flows can be readily incorporated in future studies.

"Turbulent" Levy-Lees Transformation

The viscous layer equations (Eqs. (19), (20) and (21)) can be recast in terms of similarity type variables by employing a turbulent generalization of the Levy-Lees transformation as introduced by Werle and Verdon (Ref. 4). This transformation serves to minimize the growth of the viscous layer in the computational domain and eliminate density from the formal governing equations by introducing new longitudinal and normal coordinates which are functions of density and viscosity. The new independent variables are defined by

$$\xi = \xi_1 + \int_{s_1}^{s} \rho_e \mu_e u_e g \, ds \tag{35a}$$

and

$$\eta = \frac{u_e}{\sqrt{2\xi}} \int_0^{\tilde{n}} \rho \, d\tilde{n} \tag{35b}$$

Hence the derivatives become

$$\frac{\partial}{\partial s} = \rho_e \mu_e u_e g \frac{\partial}{\partial \xi} + \frac{\partial \eta}{\partial s} \frac{\partial}{\partial \eta} \tag{36a}$$

and

$$\frac{\partial}{\partial \tilde{n}} = \rho u_e (2\xi)^{-1/2} \frac{\partial}{\partial \eta} \tag{36b}$$

Here, the definition of ξ is a simple generalization of the usual laminar Levy-Lees streamwise variable because of the introduction of the function g(s). This function can be specified (see below) to help control the thickness of the turbulent layer in the ξ,η -plane.

With new dependent variables, $F(\xi,\eta)$, $G(\xi,\eta)$, and $V(\xi,\eta)$, defined by

$$\begin{aligned} F &= u/u_e \\ G &= H/H_e \\ V &= 2\xi \left[F \frac{\partial \eta}{\partial s} + \rho \tilde{v} (2\xi)^{-1/2} \right] \Big/ \frac{d\xi}{ds} \end{aligned} \tag{37}$$

the governing equations reduce to the familiar form

continuity

$$2\xi \frac{\partial F}{\partial \xi} + \frac{\partial V}{\partial \eta} + F = 0 \tag{38}$$

ξ - momentum

$$2\xi F \frac{\partial F}{\partial \xi} + V \frac{\partial F}{\partial \eta} + \beta (F^2 - G) - \frac{\partial}{\partial \eta} \left(\ell \frac{\partial F}{\partial \eta} \right) = 0 \tag{39}$$

energy

$$2\xi F \frac{\partial G}{\partial \xi} + V \frac{\partial G}{\partial \eta} - \alpha \frac{\partial}{\partial \eta} \left[(\ell - \hat{\ell}) F \frac{\partial F}{\partial \eta} \right] - \frac{\partial \left(\hat{\ell} \frac{\partial G}{\partial \eta} \right)}{\partial \eta} = 0 \tag{40}$$

where the following notation has been introduced

$$\begin{aligned} \ell &= \rho \mu_T / (\rho_e \mu_e g) = \rho \mu (1 + \gamma_T e) / (\rho_e \mu_e g) \\ \hat{\ell} &= \rho \hat{\mu}_T / (\rho_e \mu_e g) = \rho \mu (1 + \frac{\sigma}{\sigma_T} \gamma_T e) / (\rho_e \mu_e \sigma g) \\ \alpha &= u_e^2 / \left[T_e (1 + u_e^2 / T_e) \right] \\ \beta &= \frac{2\xi}{u_e} \frac{du_e}{d\xi} (1 + \frac{u_e^2}{2T_e}) \end{aligned} \tag{41}$$

Boundary conditions for the foregoing equations are as follows (c.f. Eqs. (23) through (26)):

Edge Conditions ($\eta \to \infty$)

$$F, G \to 1 \tag{42}$$

Airfoil Surface Conditions ($\xi \leq \xi_{TE}, \eta = 0$)

$$F = V = 0 \tag{43}$$

and either

$$G = H_w(\xi)/H_e \quad \text{or} \quad \frac{\partial G}{\partial \eta} = (2\xi/Re)^{-1/2} q_w(\xi)/(\rho u_e H_e) \tag{44}$$

where $H_w(\xi)$ and $q_w(\xi)$ are prescribed functions, and ρ is a function of F, G and the fluid properties at the edge of the boundary layer as shown below

Wake Centerline Conditions ($\xi > \xi_{TE}, \eta = 0$)

$$\frac{\partial F}{\partial \eta} = \frac{\partial G}{\partial \eta} = V = 0 \tag{45}$$

Fluid properties at the edge of the boundary layer (i.e., inviscid properties at the displacement surface, $\mathcal{D}$) can be expressed in terms of the free-stream and edge Mach numbers. It follows from Bernoulli's equation, Eq. (2), that

$$(M_\infty u_e/M_e)^2 = (M_\infty A_e)^2 = (\gamma M_\infty^2 p_e)^{(\gamma-1)/\gamma} = \rho_e^{(\gamma-1)} = (\gamma-1) M_\infty^2 T_e$$
$$= \left(1 + \frac{\gamma-1}{2} M_\infty^2\right) \Big/ \left(1 + \frac{\gamma-1}{2} M_e^2\right) \tag{46}$$

and therefore

$$\alpha = (\gamma-1) M_e^2 / \left(1 + \frac{\gamma-1}{2} M_e^2\right) \tag{47a}$$

$$\beta = \frac{2\xi}{M_e} \frac{dM_e}{d\xi} \tag{47b}$$

In addition, it follows from the definition of displacement thickness, Eq. (27), the equation of state ($p = (\gamma-1)\rho T/\gamma$), and the boundary layer approximation for normal pressure gradient (i.e. $\partial p/\partial \hat{n} \sim 0$), that

$$m = \rho_e u_e \delta (Re/2\xi)^{1/2} = \int_0^\infty \left[G - F + \frac{(\gamma-1)}{2} M_e^2 (G - F^2) \right] d\eta \tag{48}$$

where m is a mass flow parameter and

$$\rho_e / \rho = G + \frac{\gamma - 1}{2} M_e^2 \left[G - F^2 \right] \tag{49}$$

Thus the explicit dependence on density can be removed from the surface heat transfer condition, Eq. (44). Finally a shear stress parameter, C_f is defined as follows

$$C_f = \frac{\tau_w^*}{\rho_\infty^* u_\infty^{*2}} = Re^{-1/2} \left(\mu \frac{\partial u}{\partial \tilde{n}} \right)\Big|_{\tilde{n}=0} = \frac{u_e^2}{(2\xi Re)^{1/2}} \left(\rho \mu \frac{\partial F}{\partial \eta} \right)_{\eta=0} \tag{50}$$

When η (or $\tilde{n}$) is normal to the airfoil surface, $\mathcal{S}$, C_f represents the surface skin friction coefficient.

Turbulence Model

The eddy viscosity model, outlined in the previous section (c.f. Eqs. (28) through (30), is rewritten in terms of the turbulent Levy-Lees variables as follows. For wall boundary layers

$$e = e_i = 0.16\, D^2 (2\xi Re)^{1/2} \rho^2 \theta^2 \mu^{-1} \left| \partial F / \partial \eta \right|, \qquad \eta < \eta_1 \tag{51a}$$

$$e = e_o = 0.0168\, \rho \mu^{-1} (2\xi Re)^{1/2} \int_0^\infty \frac{1-F}{\rho}\, d\eta, \qquad \eta \geq \eta_1 \tag{51b}$$

where η_1 is the value of η such the $e_i(\xi,\eta) = e_o(\xi,\eta)$ and

$$\theta = \int_0^\eta d\eta/\rho, \qquad D = 1 - \exp\, - \frac{\theta\sqrt{2\xi}}{a u_e}$$

$$a = 26\mu \Big/ \left[\rho Re^{1/2} (1 - 11.8 p^+) u_\tau \right] \qquad p^+ = (\mu u_e)^2 g \frac{du_e}{d\xi} \Big/ (Re\, u_\tau^3) \tag{52}$$

$$u_\tau = u_e (2\xi Re)^{-1/4} \left[\mu \frac{\partial F}{\partial \eta} \right]_{\eta=0}^{1/2} = (C_f/\rho_w)^{1/2}$$

For wakes

$$e = e_w = 0.4 (\mu u_e)^{-1} (2\xi Re)^{1/2} u_{\tau_E} \exp\left[\frac{u_e F(\xi,0)}{2.75 u_{\tau_E}} - 5.2/2.5 \right], \qquad \eta_2 < \eta < \eta_1 \tag{53a}$$

$$e = e_i\big|_{D=1} = 0.16(2\xi Re)^{1/2}\rho^2\theta^2\mu^{-1}\left|\frac{\partial F}{\partial \eta}\right|, \qquad \eta_2 < \eta < \eta_1 \tag{53b}$$

$$e = e_o, \qquad \eta > \eta_1 \tag{53c}$$

where η_2 and η_1 are the values of η such that $e_w=e_i$ and $e_i=e_o$, respectively, and the eddy viscosity is taken as e_o across the wake if $e_w>e_o$. Note that Eq. (53a) represents an approximation to the model of Eqs. (30a) and (30b) which is obtained by assuming that flow properites are constant and equal to their centerline values over the inner wake region.

The transformation function g is chosen so that the coefficient ℓ defined in Eq. (41) is approximately equal to one over most of the viscous layer. This is accomplished for example by setting

$$g = 1 + \gamma_T e_o \tag{54}$$

Thus $\ell=\rho\mu/(\rho_e\mu_e)$ for both laminar flow ($\gamma_T = 0$) and in the outer region of a fully-developed turbulent layer.

Inverse Solution Procedure

For the purpose of establishing an inverse viscous solution procedure, the following simplifications can be introduced while still retaining the essential features of the viscous boundary value problem. The flow is assumed to be adiabatic and the Prandtl numbers σ and σ_T are assumed to be unity. Thus $G(\xi,\eta) = 1$, and it is only necessary to solve the continuity and momentum equations to determine the functions F and V. In addition, the viscosity, μ^*, is assumed to vary linearly with temperature, T^*, in the viscous layer and therefore

$$\mu = T \tag{55}$$

and

$$\ell = \frac{\rho\mu(1+\gamma_T e)}{\rho_e\mu_e(1+\gamma_T e_o)} \tag{56}$$

The complete flow field is determined by an iterative procedure (see Ref. 6) which is continued until the inviscid solution at the displacement surface, $\mathcal{D}$, matches the viscous solution at the edge of the viscous layer. At each step of this process the viscous layer equations are solved numerically for prescribed mass flow parameter (or displacement thickness; c.f. Eq. (48)) and edge Mach number distributions. The continuity. Eq. (38),

and momentum (Eq. (39) with G = 1) equations are replaced by a set of linear algebraic equations using a finite difference approximation in which non-linear terms in the momentum equation are quasi-linearized, and ξ and η-derivatives are replaced by one-sided and central difference expressions, respectively (see Ref. 4). Solutions to the linear difference equations are determined by a superposition technique; i.e., new dependent variables

$$F = \beta F_I + F_{II} \tag{57}$$

$$V = \beta V_I + V_{II}$$

where

$$\begin{aligned} &F_I = 0 \text{ and } F_{II} = 1, && \eta \to \infty \\ &F_I = V_I = 0 \text{ and } F_{II} = V_{II} = 0, && \xi \le \xi_{TE}, \eta = 0 \\ &\frac{\partial F_I}{\partial \eta} \text{ and } \frac{\partial F_{II}}{\partial \eta} = 0, && \xi > \xi_{TE}, \eta = 0 \end{aligned} \tag{58}$$

are introduced so that explicit dependence on the pressure gradient parameter, β, is eliminated from the systems of equations, I and II, governing the dependent variables F_I and V_I, and F_{II} and V_{II}, respectively. The linear systems I and II, are each solved using the Davis' inversion scheme (Ref. 17).

To recover the full viscous layer solution, β must be determined for the given mass flow parameter, $m^n(\xi)$, and edge Mach number, $M_e^n(\xi)$, distributions where the superscript denotes the nth iterative estimate. It follows from Eqs. (48 with G = 1) and (57) and some algebra that β satisfies the quadratic equation

$$I_a \beta^2 + I_b \beta - I_c + m^n(\xi) = 0 \tag{59}$$

where

$$\begin{aligned} I_a &= \frac{\gamma - 1}{2} (M_e^n)^2 \int_0^\infty F_I^2 \, d\eta \\ I_b &= \int_0^\infty \left[1 + (\gamma - 1)(M_e^n)^2 F_{II} \right] F_I \, d\eta \\ I_c &= \int_0^\infty \left[1 - F_{II} + \frac{\gamma - 1}{2} (M_e^n)^2 (1 - F_{II}^2) \right] d\eta \end{aligned} \tag{60}$$

After eliminating the extraneous root, the solution of Eq. (60) is

$$\beta = (I_b/2I_a)\left[\left[1 + 4I_a(I_c - m^n)/I_b^2\right]^{1/2} - 1\right] \tag{61}$$

Once β is determined the (n + 1)th estimate (viscous) of the fluid properties at the edge of the viscous layer are obtained from the relation (c.f. Eq. (47b))

$$M_e^{n+1}(\xi) = M_e(\xi_1)\exp\left[\int_{\xi_1}^{\xi} \frac{\beta(\zeta)}{2\zeta}\, d\zeta\right] \tag{62}$$

where the subscript 1 denotes the initial station of the computational region, and Bernoulli's equation, Eq. (46). The pressure determined in this manner; i.e., p_{visc}^{n+1}, is used in conjunction with the inviscid pressure determined by Cauchy integral evaluation; i.e., Eq. (17) with $\delta(x) = \delta^n(x)$, to obtain an updated displacement thickness distribution (c.f. Eq. (32)).

NUMERICAL ALGORITHM

The basic numerical algorithm for solving the equations described in the previous sections of this report has been presented in detail by Werle and Verdon (Ref. 4). Here we seek mainly to identify those modifications and/or additions to that algorithm required for treating turbulent, separated, trailing-edge flows. First, the Cauchy solver for the inviscid pressure distribution is modified to accommodate a variable grid spacing in the streamwise direction. Second, modifications to the difference equation coefficients for the viscous equations are identified for accommodating variable grid spacing in both the streamwise and normal directions. Finally, the details of the overall solution algorithm including the mesh size and extent considerations, initialization procedures, and the overall relaxation procedure are discussed.

Inviscid Flow Representation

To accommodate a variable mesh into the difference representation of the Cauchy integral, Eq. (17), a straightforward extension of the numerical integration procedure derived by Napolitano et al. (Ref. 18) has been introduced. The slight differences that are encountered are due solely to the lack of symmetry of the variable grid with respect to the solution point. Thus, in the interaction region the Cauchy integral is approximated by

$$\frac{\pi\left[p(x_i)-p_\infty\right]}{\left(1-M_\infty^2\right)^{1/2}} = \sum_{j=i}^{I-1}\left[\frac{h'_{\mathcal{D}}(x_j)+h'_{\mathcal{D}}(x_{j+i})}{2}\right]\ln\left[\frac{x_i-x_j}{x_i-x_{j+i}}\right] + \sum_{j=1}^{I-1}\left[\frac{h'_{\mathcal{D}}(x_{j+i})-h'_{\mathcal{D}}(x_j)}{x_{j+i}-x_j}\right]\left[(x_i-x_j)\ln\left[\frac{x_i-x_j}{x_i-x_{j+i}}\right]-(x_{j+i}-x_j)\right] \tag{63}$$

where the function $h_{\mathcal{D}} = h + \delta$ defines the displacement surface, $\mathcal{D}$, the subscripts i and j denote streamwise grid point indices, and I is the index of the downstream boundary of the numerical solution domain.

To evaluate the contribution to the local pressure from displacement effects upstream of the strong interaction region; i.e.,

$$p_u(x) = -\frac{\left(1-M_\infty^2\right)^{1/2}}{\pi}\int_{x_{LE}}^{x_1}\frac{h'_{\mathcal{D}}(\zeta)}{x-\zeta}\,d\zeta \tag{64}$$

one of two approaches is employed depending on whether the flow is laminar or turbulent. For the laminar case, a square-root growth in displacement thickness is assumed and p_u is evaluated analytically. For turbulent flow,

the upstream integral is evaluated numerically with the required displacement thickness determined from a direct noninteracting boundary layer solution for the given airfoil geometry.

The contribution to the local pressure from the downstream wake; i.e.,

$$p_d(x) = -\frac{(1-M_\infty^2)^{1/2}}{\pi}\int_{x_I}^{\infty}\frac{h'_{\mathcal{D}}(\zeta)}{x-\zeta}\,d\zeta \tag{65}$$

is evaluated using the asymptotic expression

$$\delta(x) = C_1 + C_2(x-x_0)^{-1/2} \tag{66}$$

for the far-wake displacement thickness, which holds for both laminar and turbulent flow. While it is possible to relate the values of the constants, C_1, C_2 and x_0 to the airfoil properties (e.g., the airfoil drag determines C_1), a more consistent numerical solution is achieved by evaluating these constants based on the values of δ at the last three mesh points of the strong-interaction solution region. Thus, the constants in Eq. (66) can be evaluated using the following difference expressions

$$x_0 = \frac{\delta_I - \delta_{I-1} + 2\delta'_I x_I - 2\delta'_{I-1}x_{I-1}}{2(\delta'_I - \delta'_{I-1})}$$

$$C_1 = \delta_I + 2\delta'_I(x_I - x_0), \qquad C_2 = \delta_I + 2\delta'_I(x_I - x_0) \tag{67}$$

Viscous Equation Algorithm

The implicit finite difference algorithm for Eqs. (38) and (39) differs only slightly from that presented by Werle and Verdon (Ref. 4). After introducing the computational coordinates $S = S(\xi)$ and $N = N(\xi,\eta)$, Eq. (38) can be written as

$$V_j = V_{j-1} - P_j(F_j + F_{j-1}) + Q_j \tag{68}$$

where j is a normal-direction grid point index and

$$P_j = 2(\tilde{r}_{jm} + 2RS\,\tilde{h}_{jm}/\Delta S)/\Delta N$$

$$Q_j = (F_{0,j} + F_{0,j-1})\,\tilde{h}_{jm}\,RS\,\Delta N/\Delta S \tag{69}$$

The subscript 0 refers to the adjacent upstream streamwise station and

$$R = \frac{d(\ln S)}{d(\ln \xi)} = \frac{\xi}{S}\frac{dS}{d\xi}$$

$$\tilde{h}_{jm} = (\tilde{h}_{j-1} + \tilde{h}_j)/2$$

$$\tilde{r}_{jm} = (\tilde{r}_{j-1} + \tilde{r}_j)/2$$

$$\tilde{h} = \left(\frac{\partial N}{\partial \eta}\right)^{-1} \tag{70}$$

$$\tilde{r} = \tilde{h}\left[1 - \frac{\partial}{\partial \eta}\left[2SRh\frac{\partial N}{\partial S}\Big|_{\eta}\right]\right]$$

Similarly, the momentum Eq. (39) can be written as

$$A_j F_{j-1} + B_j F_j + C_j F_{j+1} + D_j V_j = \tilde{\beta} E_{1_j} + E_{2_j} \tag{71}$$

where

$$A_j = \tilde{e}_{jm}/(\Delta N)^2 + C_N V_{r_j}/(4\Delta N)$$

$$B_j = -2Rh_j SC_R F_{r_j}/\Delta S - (\tilde{e}_{jp} + \tilde{e}_{jm})/(\Delta N)^2$$

$$C_j = \tilde{e}_{jp}/(\Delta N)^2 - C_N V_{r_j}/(4\Delta N)$$

$$D_j = (C_N/2 - 1)(F_{r_{j+1}} - F_{r_{j-1}})/(2\Delta N)$$

$$E_{1_j} = Rh_j(F_{r_j}^2 - 1)$$

$$E_{2_j} = -2Rh_j C_R S\left[C_L(2-C_L)F_{0j}^2 + (1-C_L)(2-C_L)/(2F_{2j}^2)\right]/\Delta S + C_L(C_L-1)F_j F_{0j}/2$$

$$\tilde{\beta} = R\beta$$

$$\tilde{e}_{jp} = (\tilde{e}_{j+1} + \tilde{e}_j)/2$$

$$\tilde{e}_{jm} = (\tilde{e}_j + \tilde{e}_{j-1})/2$$

$$\tilde{e} = \ell \tilde{h}^{-1}$$

$$F_{r_j} = C_L(2-C_L)F_{0j} + (1-C_L)(2-C_L)/(2F_{2j}) + C_L(C_L-1)/(2F_{0j})$$

$$V_{r_j} = C_L V_{0j} + (1-C_L)V_{2j} \tag{72}$$

with

$$C_L = \begin{cases} 0 \text{ implies forward linearization and convective differencing}^* \\ 1 \text{ implies backward linearization and convective differencing} \\ 2 \text{ implies backward iterative linearization and convective differencing} \end{cases} \tag{73a}$$

$$C_R = \begin{cases} 1 \text{ for forward flow} \\ -1 \text{ for reverse flow} \end{cases} \tag{73b}$$

The coefficient C_N refers to the coupling of the continuity and momentum equations through the linearization of the normal convective term.

$$C_N = \begin{cases} 0 \text{ refers to the first-order linearization, equations coupled} \\ 1 \text{ refers to second-order linearization, equations coupled} \\ 2 \text{ refers to first-order linearization, equations uncoupled} \end{cases} \tag{73c}$$

* These values were incorrectly given in reverse order in Ref. 4

For the present applications, the options used were $C_L = 1$, $C_R = 1$, and $C_N = 1$ except in reverse flow regions where C_L and C_R were set equal to 0 and -1, respectively. For the flat-plate cases where a singularity is known to exist at the trailing-edge point, the difference equations were adjusted for a first-order coupled linearization ($C_N = 0$) and a backward convective approximation with the velocity coefficient linearized about the previous iteration level ($C_L = 2$). All remaining aspects of the viscous solution algorithm are identical to those presented in Ref. 4.

General Solution Algorithm

The computational coordinates are defined using geometric progressions to allow a packing of grid points in regions of large flow gradients. In the normal direction, the general expression used for setting the mesh spacing and hence $\tilde{h}(\eta)$ is

$$\eta = \eta_{max}\left[1-K^{N/\Delta N}\right]\Big/\left[1-K^{\eta_{max}/\Delta N}\right] \tag{74}$$

where K is the mesh spacing constant, η_{max} is the value of the turbulent Levy-Lees variable, η, at the outer edge of the viscous layer and ΔN is the normal grid spacing in the computational plane. For the cases considered here forty grid points have been used in the normal direction, and as shown by Carter, Edwards, and Werle (Ref. 19) the value of η_{max} can be set at 10 for virtually all flows - be they laminar, transitional or turbulent. Selection of the mesh spacing parameter, K, is based on fluid dynamic requirements. For laminar flows, K is prescribed so that the first grid point from the lower boundary is at the same physical position as its triple-deck solution counterpart (c.f. Ref. 4). It was found that this could be accomplished using a simple uniform spacing; i.e., K = 1. For turbulent flow, mesh streching is used to capture the anticipated sub or inner layer of the viscous region. It was found that using a value of K = 1.05 provided sufficient resolution of the inner layer for the turbulent cases considered herein.

Establishment of a longitudinal grid spacing involved two steps. First, the separation coordinate curve, $\mathcal{S}$, is positioned, and then a grid distribution is defined using a double geometric progression centered at the trailing edge. Since only first derivatives in the streamwise direction appear in the governing equations, it is only necessary to provide a means of locating the individual grid points. To this end the following scheme was applied. For

$x<x_{TE1}(1 = 2, \ldots, i_{TE1})$

$$x_i = x_1 + (x_{TE} - x_1)(1 - K_u^{(i-1)}) / (1 - K_u^{(i_{TE}-1)}) \tag{75a}$$

and for $x \geq x_{TE1}$ $(i = i_{TE1}, \ldots, I)$

$$x_i = x_{TE1} + (x_{TE1} - x_{TE})(1 - K_d^{(i-i_{TE1})}) / (1 - K_d^{(I-1)}) \tag{75b}$$

where the subscripts TE and TE1 refer to grid point locations at the trailing edge and immediately downstream of the trailing edge, respectively. The parameters used to adjust the upstream grid spacing are the spacing parameter, K_u, the number of points, i_{TE}, and the overall length, $x_{TE} - x_1$. For the downstream region, the only parameters available are the spacing constant, K_d, and the total number of points, I, since here the overall length is established from the value of $x_{TE1} - x_{TE}$ which is set by the upstream expression. For the current calculations x_1 was generally set equal to 0.4 with 41 grid points ahead of the trailing edge. Downstream 41 points were again used over a distance of approximately 0.6. For laminar flows, grid stretching was not applied in the streamwise direction while for several of the turbulent flow cases, K_u and K_d were set equal to 0.95 and 1.05, respectively. For blunt trailing-edge geometries, the shear-layer coordinates (Fig. 1) are employed. The mesh stretching is then centered around the shear-layer coordinate trailing-edge point which is located at the intersection of the shear-layer coordinate curve and the normal coordinate line which passes through the trailing edge point.

As depicted in the sketch below, the shear-layer coordinate curve was taken as a three piece fit with the airfoil surface forming the initial segment $(x \leq x_2)$, followed by a cubic section for $x_2 \leq x \leq x_4$ which is tangent to the airfoil surface at the point x_2 and to the wake centerline at the point x_4, and with the wake centerline forming the third segment for $x > x_4$. The trailing-edge region cubic is established such that the trailing-edge location on the s-coordinate curve is positioned at a prescribed ratio, r, of the distance from x_2 to x_4. That is, x_4 is set according to the relation

$$r = (x_3 - x_2)/(x_4 - x_2) \tag{76}$$

and the value of x_3 is computed for a given cubic using the relation

$$x_3 - x_2 = \frac{1}{2}\left[x_{TE} - x_2 + \sqrt{(x_{TE}-x_2)^2 + 24\,h(x_2)\,r^2(1-r)\left[1+r^2(2r-3)\right]}\,\right] \tag{77}$$

Here r was set equal to 0.5 for all cases studied.

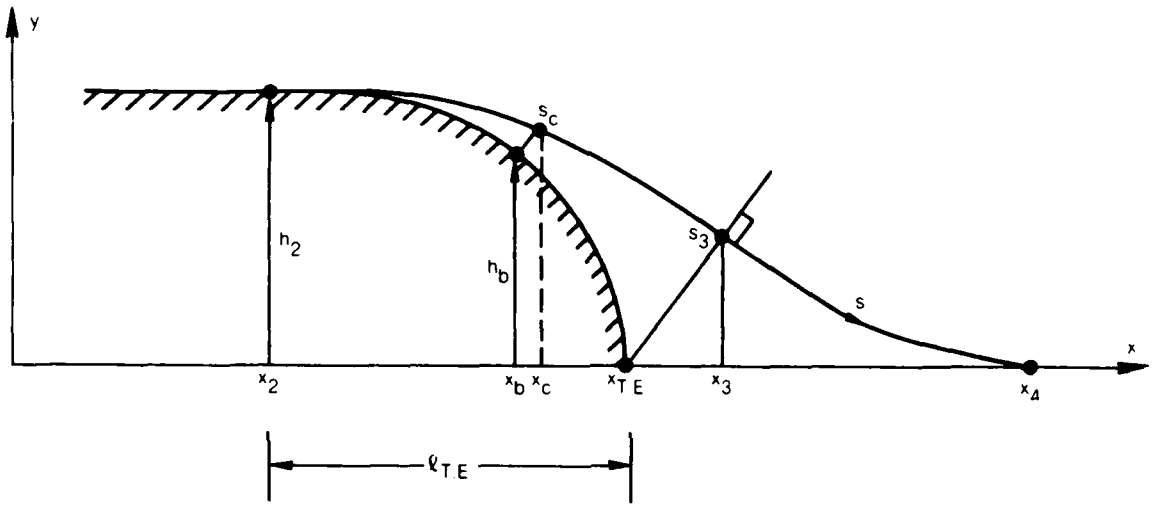

The s-coordinate curve is then positioned according to the relation

$$h_s(x_2) = h(x_2)\left[\left(\frac{x-x_2}{x_4-x_2}\right)\left[2\,\frac{x-x_2}{x_4-x_2} - 3\right] + 1\right] \tag{78}$$

and the coordinate surface inclination angle is given by

$$\tilde{\phi}_c = \tan^{-1}\left[\frac{6h(x_2)}{x_4-x_2}\left(\frac{x-x_2}{x_4-x_2}\right)\left(\frac{x-x_2}{x_4-x_2} - 1\right)\right] \tag{79}$$

Finally, there is a need to establish the airfoil height, $h(x_b)$, at a coordinate location s_c; i.e.,

$$h(x_b) = \left[\tilde{b}^2 - 2\tilde{a}\,(x_b - x_{TE}) - \tilde{c}\,(x_b - x_{TE})^2\right]^{1/2} - \tilde{b} \tag{80a}$$

where

$$x_b = x_{TE} + \frac{(\tilde{d} - \tilde{a}\tan^2\tilde{\phi}_c) + \left[(\tilde{d}^2 - \tilde{a}\tan^2\tilde{\phi}_c)^2 - (1+\tilde{c}\tan^2\tilde{\phi}_c)(\tilde{d}^2 - \tilde{b}^2\tan^2\tilde{\phi}_c)\right]^{1/2}}{1 + \tilde{c}\tan^2\tilde{\phi}_c} \tag{80b}$$

with

$$\begin{aligned} \tilde{a} &= \ell_{TE}(h_0/\ell_{TE})^2\,\tilde{\gamma}/(\tilde{\gamma}-2) \\ \tilde{b} &= h_0/(\tilde{\gamma}-2) \\ \tilde{c} &= (h_0/\ell_{TE})^2\,\tilde{\gamma}/(\tilde{\gamma}-2) \\ \tilde{d} &= x_c - x_{TE} + (h(x_c)+\tilde{b})\tan\tilde{\phi}_c \\ \tilde{\gamma} &= \ell_{TE}\tan\alpha_f/h_0 \end{aligned} \tag{80c}$$

To apply the present iterative solution procedure, it is necessary to establish initial estimates to the displacement surface and the boundary layer profile at the upstream boundary, $x = x_1$, of the computational domain. This information was determined using the viscous solution algorithm in the direct mode which provides the required velocity profile and displacement thickness distribution for a specified pressure distribution. This imposed pressure distribution was calculated using the inviscid pressure Eq. (17), with the shear-layer coordinate curve taken as the first estimate to the displacement surface. With the resulting pressure distribution, a marching viscous solution proceeds from the leading edge of the airfoil to the upstream boundary, $x = x_1$, of the strong-interaction region to establish the initial velocity profile and the displacement contribution to the upstream pressure integral, Eq. (64). For a flat-plate airfoil this initial marching solution is unnecessary since a self-similar boundary layer solution can be determined.

Subsequent interative passes through the inviscid and viscous solutions proceeded with a relaxation factor, ω, generally held at a value near unity, to achieve a converged solution in which the displacement surface ceased to vary in the 4th significant figure. For some of the larger separation bubble cases, this level of convergence required approximately 50 iterations, with a relaxation factor of 1/3.

APPLICATION TO TRAILING-EDGE FLOWS - RESULTS AND DISCUSSION

The analytical and numerical approach outlined above has been assessed through a series of model problem studies. The first series focused on laminar flat-plate trailing-edge flow to provide a fundamental assessment of the present approach through detailed comparisons with triple-deck solutions. The second test series considered the extension of the interacting boundary layer (IBL) approach to laminar blunt-based configurations where again triple deck solutions are available for comparison. The third study involved the introduction of turbulence effects with initial focus on flat-plate trailing-edge flow where limited data is available for assessment. The final test series considered application of the interacting boundary layer approach to turbulent blunt-based flows-including separation phenomena.

Laminar Flow

Flat-Plate Triple-Deck Solutions

As discussed in Ref. 4, the basic numerical algorithm employed in the interacting boundary layer analysis is a direct extension of the numerical method developed in Ref. 4 for the solution of the triple-deck, asymptotic-limit ($Re \to \infty$), form of the governing equations. It is thus imperative that this triple-deck algorithm first be assessed by comparison of results with those of other investigators (e.g., Refs. 20 and 21). The problem of calculating the laminar solution for the trailing-edge region of a flat plate imposes a severe test to a numerical solution algorithm because of the occurrence of a fundamental singularity in the pressure gradient at the trailing edge. Current results, obtained with the basic algorithm (designated by the solid curve in Fig. 2) compare very favorably with those of Refs. 20 and 21 up to the trailing edge but significant differences occur along the wake (c.f., Fig. 2). Note that the pressure, P, and distance, X, (Fig. 2) are dimensionless variables which have been scaled according to triple-deck scaling laws. There are numerous possible sources for this discrepancy, ranging from truncation errors to an inaccurate representation of the trailing-edge singularity (see Ref. 20 for a detailed discussion of this). Of these, it was found that the most influential was the manner in which the viscous pressure distribution was determined. If p_{visc} is obtained by a forward-marching integration across the mesh element just aft of the trailing edge, the singularity at the trailing edge will not be properly accounted for. To avoid this error, solutions have been obtained with a forward-marching integration up to the trailing edge and a backward-marching integration (from the downstream asymptotic solution) to the mesh element just aft of the trailing edge. Wake pressure distributions

determined with this new integration scheme (Fig. 2(a)) are in better agreement with those of previous investigators. The remaining differences are attributed to truncation error, as demonstrated in Fig. 2(b), which shows the approach of the current trailing-edge region pressure distributions toward the analytic predictions of Ref. 20 as the longitudinal grid spacing is reduced from ΔX = 0.2 to 0.05. It is important to note that in both Refs. 20 and 21, special analytical adjustments were applied at the trailing edge.

Flat-Plate, Finite-Reynolds-Number Solutions

Interacting boundary layer solutions have been determined to verify their systematic approach to the triple-deck limit solution as $Re \to \infty$. For this purpose, two separate studies have been conducted. In the first, the forward/reverse viscous pressure integration discussed relative to Fig. 2 was employed and in the second, the forward-marching integration was used. The resulting comparisons of the IBL solutions with their respective triple-deck solutions are shown in Figs. 3(a) and 3(b) for a longitudinal step size of ΔX = 0.2. The IBL solutions were obtained with the physical mesh spacing adjusted so that ΔX = 0.2 and the variable normal grid spacing set such that the spacing in the inner region of the viscous layer corresponded to ΔY = 0.4, where Y is the triple-deck normal coordinate. As shown in Figs. 3(a) and 3(b), the resulting IBL solutions show a systematic approach to their respective triple-deck counterparts. While in an overall sense, these results verify the IBL algorithm, they also indicate that the trailing-edge singularity is causing complications that must be addressed. The Davis (Ref. 22) algorithm apparently avoids these complications and consideration should be given to adopting several features of his approach in our future studies.

One aspect of the interacting boundary layer solution which was found to be of paramount importance is the contribution to the pressure in the strong-interaction region from displacement effects upstream and downstream of this region (c.f., Eqs. (64) and (65)). To illustrate this point, solutions have first been determined for a flat plate of infinite extent where formal weak-interaction theory predicts that the pressure coefficient, $C_p = p - p_\infty$, is zero over the length of the plate. Solutions obtained for $Re = 10^5$ with the computational region extending from s = x = 0.4 to s = x = 1.6 are shown in Fig. 3(c). A comparison of the solutions with and without the far-field contributions, p_u and p_d, to the local pressure clearly shows the significant impact of these terms at this Reynolds number. Figure 3(c) also compares solutions for a finite flat plate obtained with and without the far-field contributions to the local pressure. The results indicate rather large differences especially near the computational boundaries. Clearly, far-field, weak-interaction phenomena can be expected to have a significant impact on solutions determined in local strong-interaction regions.

Solutions to the interacting boundary layer equations for a finite flat plate at a Reynolds number of 10^5 have also been presented by Davis (Ref. 22) and Veldman (Refs. 23-25). Their results are compared with the present solution in Figs. 4(a) through 4(c). Veldman's solutions, based on a composite boundary-layer/triple-deck model and on the interacting boundary layer model were obtained without accounting for far-field displacement effects on the upstream flow as discussed above. Thus, it is not surprising that considerable differences exist between predicted upstream pressure levels (Fig. 4(a)). However, present results compare very favorably with the recent results of Davis (Ref. 22) which were obtained with global far-field effects accounted for. Only minor differences (Fig. 4(a)) occur just aft of the trailing edge where very steep gradients are encountered. Based on the mesh size study described above, one would expect these differences to vanish with decreasing mesh spacing.

Results for skin friction, wake centerline velocity, and displacement thickness distributions are presented in Figs. 4(b) and 4(c). The various interaction solutions are seen to be in excellent agreement. Also shown are the "noninteracting" results obtained from the boundary layer/wake equations with the imposed inviscid pressure gradient taken to be zero. The noninteracting displacement thickness distribution, Fig. 4(c), has a square-root growth up to the trailing edge followed by a rapid (singular) drop-off in the wake just aft of the trailing edge, which is due to the change in surface boundary condition at the trailing edge. The singularity at the trailing edge is relieved when strong-interaction effects are accounted for (IBL analysis). It can be seen that the strong interaction at the trailing edge is felt upstream up to approximately $x = 0.75$ and that it significantly alters the displacement thickness gradient in the near wake ($1.0 \leq x < 1.25$). Seen in this light, the strong-interaction region appears to be confined to the region $0.75 < x < 1.25$ where it provides a local correction to the global near-wake neck-down effect. This strong interaction causes an acceleration and thinning of the boundary layer near the trailing edge (Fig. 4(c)) with a subsequent increase in surface shear stress (Fig. 4(b)).

Blunt Trailing-Edge Solutions

The present numerical scheme has been applied to blunt trailing-edge flows typical of those encountered in turbomachinery applications. A shear-layer coordinate system has been established and calculations have been performed for laminar flows past thickened flat-plate airfoils ($\alpha_w = 0$) with elliptic-section trailing edges (see Fig. 5(a)). Converged solutions have been obtained for attached and separated flows at Reynolds numbers (based on plate length) of 10^5 and 10^7 which will be shown to approach their triple-deck limits with increasing Re for attached and

mildly separated flows. Sample results for a free-stream Reynolds number of 10^5 and Mach number of 0.1 with an elliptic section length, ℓ_{TE}, of 0.2 and heights, h_o, of 0.07 and 0.14 are shown in Figs. 5(a) through 5(f). These parameters give an inner deck scaling of $L = 4$, $H_0 = 4$ and 8, and $\gamma = 2$, and thus correspond to two of the triple-deck solutions reported in Ref. 4. The interacting boundary layer solutions were obtained for a strong-interaction calculation region extending from 40 percent chord to 160 percent chord. Classical Blasius boundary layers and Goldstein wakes were assumed to exist upstream and downstream, respectively, of the interaction region. The shear-layer coordinate curve was taken as a simple cubic (see Fig. 5(b)), tangent to the airfoil at the trailing-edge juncture point and to the wake centerline at 140 percent chord.

In the resulting solutions (Figs. 5(b) through 5(f)) the displacement surfaces show steady growth up to near the juncture point followed by a rapid smooth decay in the near wake toward constant far-wake values (Fig. 5(b)). The surface skin friction and wake centerline velocity distributions are shown in Fig. 5(c) where the thick blade case, $H_0 = 8$, is seen to experience considerable separation off the blunt base. The oscillations in the skin friction at the upstream boundary of the interaction region are due to the rapid adjustment of the assumed initial self-similar velocity profile to a compatible nonsimilar state. The thick plate case experiences a skin friction growth immediately downstream of the initial station which is due to boundary layer thinning induced by a flow overspeed as it accelerates around the elliptic trailing edge.

The displacement thickness distribution over the trailing edge region (c.f., Fig. 5(d)) has a singularity at the trailing edge point. If the shear-layer coordinate curve (c.f., Fig. 5(b)) were taken to coincide with the airfoil surface; i.e., $t = 0$, then the classical first-order inviscid flow would be singular at the trailing edge. The current approach eliminates this singularity by defining a smooth coordinate surface in such a fashion that the blunt trailing-edge singularity is removed from the first-order inviscid solution. It should be noted that the shear-layer coordinate concept has been recently applied by Carter et al., (Ref. 26) for solution of the transonic shock-induced separation problem. This application represents one of the major contributions of the current effect.

The pressure distributions for the blunt trailing-edge geometries are shown in Figs. 5(e) and 5(f). For these cases, the pressure levels from the successive inviscid and viscous calculations converge relatively slowly in the near-wake region. This is illustrated in Fig. 5(f) where the respective inviscid and viscous pressure levels are shown after 50 iterations. However, it was found that the mean pressure distribution (as shown in Fig. 5(e)) was well converged after only 20 iterations and that both the

inviscid and viscous pressures headed toward this level. This result indicates that the iteration scheme might be improved through use of an averaging technique.

The pressure distributions depicted in Fig. 5(e) show initial pressure levels significantly different from their flat-plate counterpart (see Fig. 4(a)). This is due both to the blunt geometry and global weak-interaction effects. As discussed above, the initial pressure level is established by adding the global weak-interaction contribution (i.e., the far-field contribution to the pressure in the strong-interaction region) to the geometric-induced pressure level. The pressure drop downstream of the initial station is caused by the flow acceleration around the blunt trailing edge. There is a rapid pressure rise across the trailing edge to a near-wake peak value followed by a weak-interaction pressure decay in the far wake. The appearance of a "plateau" like region for the separated case, $H_o = 8$, leads to a pressure signature in the near wake region quite similar to that observed in experimental studies of bluff-based bodies. It is surprising to find a very fine scale pressure-gradient reversal at trailing edge for the separated case and it has not been established whether this is realistic or merely a feature of the present interaction model.

A final assessment of the interacting boundary layer code for blunt trailing edges is obtained through comparison with the triple deck solutions of Ref. 4. The only available basis for assessing the current blunt airfoil solutions is to ascertain whether they approach corresponding triple-deck solutions as the Reynolds number is increased. To perform such a study it is necessary to adjust the scale of the physical geometry and finite difference mesh such that they honor the triple-deck scaling laws. Figures 6(a) through 6(c) present the results of such a study for two thicknesses, $H_o = 4$ and $H_o = 8$, as $Re \to \infty$. The results have been presented in triple-deck variables with the asymptotic solutions ($Re \to \infty$) taken directly from Ref. 4. In general, the results show a relatively insensitive dependence on Reynolds number indicating that the asymptotic solution, $Re \to \infty$, can be used to obtain good qualitative and quantitative predictions for a Reynolds number as low as 10^5. This result is in sharp contrast to the supersonic separated flow results obtained by Burggraf et al., (Ref. 27) where the density variations across the inner layer severely limited the range of applicability of triple-deck theory.

Considering the specific results of this study, attention is first directed to the unseparated case, $H_o = 4$. The IBL results show a slow but systematic approach to the triple-deck solution over the entire solution domain (Fig. 6(a)). The accompanying shear stress and wake centerline velocity distributions (Fig. 6(b)) behave similarly except near the initial

station (X = -6) of the computational region. Such behavior is believed to be traceable to the initialization procedure. For the IBL results, the mesh spacing was determined such that in triple-deck variables it was fixed at $\Delta X = 0.1$ as $Re \to \infty$. For the fixed number of longitudinal mesh points used in the current study (121), this corresponded to an upstream boundary at X = -6. Apparently this location is too close to the trailing edge to allow the use of a self-similar velocity profile to start the calculation. Fortunately, initial errors appear to damp out rather quickly.

The situation is slightly changed for the thicker airfoil, $H_o = 8$. Again there is an anamoly in shear stress near the initial station, X = -6, (Fig. 6(c)) but this effect quickly disappears as X increases. A notable difference occurs in the wake region where the pressure (Fig. 6(a)) and wake-centerline velocity (Fig. 6(c)) distributions show a small but distinct sensitivity to Re in the near wake. Note that, as in the $H_0 = 4$ case, the starting procedure apparently causes a nonuniformity in the behavior of pressure and skin friction with increasing Reynolds number over the interval $-4<X<-1$ (as shown in Figs. 6(a) and 6(c)).

Turbulent Flow

Application of the current analysis to the case of turbulent trailing-edge flows was accomplished using the eddy viscosity formulation outlined in Eqs. (28) through (30). This eddy viscosity model has been expressed in terms of the "turbulent" Levy-Lees type variables, Eqs. (51) through (53), in which the longitudinal independent variable is defined in such a manner as to minimize the effects of turbulence on the growth of the viscous region in the computational domain. In addition, the Levy-Lees normal coordinate has been scaled to provide more mesh points near the wall and wake centerline so that a better resolution of the turbulent inner layer and also of thin separation bubbles can be obtained.

For the turbulent cases, the pressure contribution from the region ahead of the strong-interaction zone (Eq. (64)) cannot be evaluated analytically. Thus the upstream displacement thickness distribution was taken directly from classical non-interacting boundary layer calculations with instantaneous transition imposed immediately aft of the leading edge. The appropriate far-wake displacement thickness distribution is of the Goldstein square-root decay type and thus the procedure employed for the laminar case carried over directly.

Flat-Plate Trailing Edge

After the turbulence model and the variable mesh spacing capability were incorporated into the finite Re interaction algorithm, a viscous/inviscid interaction solution was determined for subsonic turbulent flow

at $M_\infty = 0.0116$ and $Re = 6.5 \times 10^5$ past a flat-plate trailing edge. The viscous/inviscid interaction pressure distribution for this case is shown in Fig. 7(a) along with a prediction based on a second-order, noninteracting, boundary-layer solution. The noninteracting solution was determined over the length of the plate and into the wake region to obtain a first-order displacement thickness distribution. In the spirit of higher-order boundary layer corrections, the inviscid pressure distribution was then calculated based on this displacement thickness distribution. The result shown in Fig. 7(a) reveals an expected singular behavior at the trailing edge. The interaction solution indicates that the displacement interaction effect is highly confined to near the trailing edge point, as anticipated by Melnik (Ref. 1), and serves principally to remove the pressure discontinuity at the trailing edge. The conclusion drawn here is that while strong interaction effects are important, they do not dominate weak, global interaction effects except in the immediate vicinity of the trailing edge.

Present results for wake centerline velocity are compared with data taken by Chevray and Kovasznay (Ref. 28) and results of the noninteracting solution of Cebeci et.al. (Ref. 15) in Fig. 7 (b). It can be seen that the agreement between the noninteracting and interacting solutions and the data is very good. Important features are that the interacting solution gives a slight improvement over the noninteracting results in the near wake, and that both solutions underpredict the wake-centerline velocity in the far wake. Such differences are well within the uncertainty surrounding the turbulence model for trailing-edge flow.

Blunt Trailing Edge

The final cases presented here are those for turbulent flow off the trailing edge of a thickened flat plate airfoil. The geometry, Reynolds number, and Mach number are identical to those studied for laminar flow (c.f., Figs. 5(a) and 6). The resulting displacement body and surface pressure distributions for $H_o = 4$ are compared to their laminar counterparts in Figs. 8(a) through 8(c). The turbulent results show steeper gradients in displacement thickness and pressure across the trailing-edge region than those encountered in the laminar case. This results in a slightly higher peak pressure in the near wake. The far-wake displacement thickness is larger for turbulent than for laminar flow, which is apparently due to the increased drag induced on the airfoil in the turbulent case. It is interesting to note the degree to which the local interaction effect influences the pressure distribution. The rapid decrease in displacement thickness in the near wake so dominates the problem that significant differences between laminar and turbulent pressure distributions can only be detected over a relatively small region of the near wake.

Results indicating the effect of airfoil thickness on turbulent trailing-edge flows are shown in Figs. 9(a) through 9(c). The strong interaction solutions were initiated at a 40 percent chordwise station with the initial boundary layer profiles determined from noninteracting solutions upstream of this region. Minor nonuniformities appear in the skin friction parameter and pressure distributions of Figs. 9(b) and 9(c) near the initial station because trailing-edge interaction effects apparently do not fully attenuate at this upstream location. The far-wake displacement thickness was again represented asymptotically as a square-root decay to a constant level. The constants of this asymptotic representation were determined by the strong-interaction solution. As shown in Fig. 9(a), the shear-layer coordinate curve was set tangent to the airfoil surface at the trailing-edge juncture point and to the wake centerline at 125 percent chord.

The displacement surface predictions are shown in Fig. 9(a) where a steady growth is indicated up to the trailing-edge juncture point, followed by a very rapid thinning into the near wake, and then a gradual thinning toward constant levels in the far wake. Note that the distorted scale of Fig. 9(a) tends to over-dramatize this effect and that true flow angles are much less severe than those shown. It is surprising to find that the far-wake displacement body approaches the same constant level for the two cases even though these displacement bodies differ by as much as 70 percent at the strong-interaction initiation point. This can be explained to some extent by a consideration of the asymptotic wake structure. The wake displacement thickness is a direct function of airfoil drag. Since the airfoils are of similar geometry, one would expect and Fig. 9(b) verifies, that the skin friction drag would be nearly identical for the two cases. The only difference then must be traceable to the immediate trailing-edge region, which is physically of very small extent.

The skin friction parameter and wake centerline velocity distributions of Fig. 9(b) indicate very small differences over the entire trailing-edge region with only a very mild separation occurring for the thick airfoil (H_o = 8). However, the pressure distributions of Fig. 9(c) do show interesting and significant differences. There are three major contributions to this pressure difference; first, that due to geometric differences which sets overall lower surface and higher wake pressures for the thick airfoil; second, the global weak interaction contribution from the finite-thickness, far-wake displacement body which mitigates the geometric differences; and finally, the near-wake strong-interaction effects which serve to bridge the differences between the respective surface and wake pressure distributions.

CONCLUSIONS AND RECOMMENDATIONS

A general approach based on viscous/inviscid interaction theory has been outlined for determining high Reynolds number flow past a cascade of airfoils. The overall flow field is broken down into "inner" dissipative fields consisting of attached boundary layers, wakes, and local strong-interaction (possibly separated) flow regions and an "outer" inviscid field. The flow in the inner or viscous regions is assumed to be governed by Prandtl's boundary layer equations and the outer flow is assumed to be isentropic and irrotational (i.e., the Interacting Boundary Layer Model). Solutions to the viscous and inviscid equations are matched to provide a solution for the entire flow field. The matching procedure depends on the nature (i.e., weak or strong) of the interaction between the inviscid and viscous flows.

In the present study emphasis has been placed on the development of a solution procedure for local strong-interaction regions and, in particular, the strong-interaction region caused by the change in boundary condition experienced by the fluid as it leaves the surface at the trailing edge of an airfoil. Subsonic laminar and turbulent flows past sharp and blunt trailing edges have been considered. A shear-layer coordinate, which departs from the airfoil surface upstream of the trailing edge and "reattaches" on the wake centerline, has been introduced for blunt-edge applications. After making the usual thin viscous layer assumptions relative to the shear-layer coordinate system and applying Prandtl's transposition theorem, the classical form of the boundary layer equations is retained. These equations are then recast in terms of "turbulent" Levy-Lees variables to facilitate numerical resolution. For strong viscous/inviscid interactions an iterative solution procedure is required. In the present effort successive inviscid and viscous solutions are determined directly and inversely, respectively; i.e., the displacement thickness is prescribed and the two governing equation sets are solved to determine the inviscid and viscous pressure fields. Updated values of displacement thickness are obtained using Carter's (Ref. 6) relaxation procedure until a converged solution for the overall flow field is achieved.

Numerical results have been presented here for symmetric adiabatic flows past thin-airfoil trailing edges. Laminar flat-plate results are in very good agreement with those of other investigators (Refs. 22 and 23). In addition, the present finite Reynolds number solutions approach asymptotic ($Re \to \infty$) triple-deck solutions (Refs. 20 and 21) with increasing Reynolds number. Separated laminar flow solutions have been determined for thickened flat-plate airfoils with elliptic-section trailing edges. These blunt-edged results also approach triple-deck solutions (Refs. 4 and 5) with increasing Reynolds number. Turbulent flows past flat-plate and thickened flat-plate airfoils have also been calculated. For these cases, no other interaction solutions are available for

assessing the current analysis. However, present results for wake-centerline velocities behind a thin flat-plate airfoil have been found to be in good agreement with the experimental data reported by Chevray and Kovasznay (Ref. 28).

In the present effort, consideration has been restricted to symmetric flows, and hence, a primary goal in future work will be the extension of the present concepts and solution procedures to asymmetric trailing-edge flows which are representative of those encountered in turbomachinery applications. In addition, there is a need for assessing the current analysis through comparison with experimental measurements of pressure and velocity distributions in the turbulent near-wake region of a symmetric airfoil. Finally, the existing numerical solution procedure should be further developed to improve the resolution of flows with relatively large separation regions, and to improve the convergence rate of the viscous/inviscid iteration procedure. One possibility here is to incorporate the quasi-simultaneous iteration procedure developed by Veldman (Ref. 8) and Davis (Ref. 22) into the present solution algorithm.

REFERENCES

1. Melnik, R. E., R. Chow, and H. R. Mead: Theory of Viscous Transonic Flow over Airfoils at High Reynolds Number. AIAA Paper No. 77-680, presented at the Tenth Fluid and Plasma Dynamics Conference, Albuquerque, New Mexico, June 27-29, 1977.

2. Verdon, J. M. and M. J. Werle: Development of a Viscous Transonic Cascade Analysis. United Technologies Research Center Report R78-912864-6, prepared under Contract N00019-77-C-0242 for the Naval Air Systems Command, October 1978.

3. Werle, M. J., and J. M. Verdon: Solutions for Supersonic Trailing Edges Including Separation. AIAA Paper No. 79-1544, presented at the 12th Fluid & Plasma Dynamics Conference, Williamsburg, Va., July 24-26, 1979.

4. Werle, M. J. and J. M. Verdon: Viscid/Inviscid Interaction Analysis for Symmetric Trailing Edges. United Technologies Research Center Report R79-914493-5, prepared under Contract N00019-78-C-0604 for the Naval Air Systems Command, January 1980.

5. Werle, M. J. and J. M. Verdon: Solutions for Laminar Subsonic Trailing Edge Flows at Asymptotically Large Reynolds Numbers. Paper presented at the International Conference on Boundary and Interior Layers, held at Trinity College, Dublin, Ireland, June 3-6, 1980.

6. Carter, J. E.: A New Boundary Layer Interaction Technique for Separated Flows. AIAA Paper No. 79-1450, presented at the 4th Computational Fluid Dynamics Meeting, Williamsburg, Virginia, July 23-24, 1979.

7. Melnik, R. E.: Turbulent Interactions on Airfoils at Transonic Speeds-Recent Developments. AGARD Symposium on Computation of Viscous-Inviscid Flows, AGARD-CPP-291, 1980, Chapter 10.

8. Veldman, A.E.P.: The Calculation of Incompressible Boundary Layers with Strong Viscous-Inviscid Interactions, AGARD-CPP-291, 1980, Chapter 12.

9. Caspar, J. R., D. E. Hobbs, and R. L. Davis: Calculation of Two-Dimensional Potential Cascade Flow Using Finite Area Methods. AIAA Journal, Vol. 18, January 1980, pp. 103-109.

10. Ives, D. C. and J. F. Liutermoza: Second Order Accurate Calculation of Transonic Flow over Turbomachinery Cascades. AIAA Journal, Vol. 17, August 1979, pp. 870-876.

REFERENCES (Cont'd)

11. Blottner, F. G.: Computational Techniques for Boundary Layers. AGARD Lecture Series 73 on Computational Methods for Inviscid and Viscous Two- and Three-Dimensional Flow Fields, presented at the Von Karman Institute, February 17-22, 1975.

12. Verdon, J.M. and J. R. Caspar: Subsonic Flow Past an Oscillating Cascade with Finite Mean Flow Deflection. AIAA Journal, Vol. 18, No. 5, May 1980, pp. 540-548.

13. Caspar, J.R. and J. M. Verdon: Numerical Treatment of Unsteady Subsonic Flow Past on Oscillating Cascade. Paper No. 80-1428, presented at the AIAA 13th Fluid & Plasma Dynamics Conference, Snowmass, Colorado, July 14-16, 1980.

14. Cebeci, T. and Smith, A.M.O.: Analysis of Turbulent Boundary Layers. Academic Press, New York, 1974.

15. Cebeci, T., Thiele, F., P. G. Williams and K. Stewartson: On The Calculation of Symmetric Wakes 1. Two Dimensional Flows. Numerical Heat Transfer, Vol. 2, pp. 35-60, 1979.

16. Harris, J.E.: Numerical Solution of the Equations for Compressible, Laminar, Transitional, and Turbulent Boundary Layers and Comparisons with Experimental Data. NASA TR-R-368, August 1971.

17. Werle, M.J. and S. D. Bertke: A Finite Difference Method for Boundary Layers with Reverse Flow. AIAA Journal, Vol. 10, No. 9, pp. 1250-1252, September 1972.

18. Napolitano, M., M. J. Werle and R. T. Davis: A Numerical Technique for the Triple-Deck Problem. AIAA Paper No. 78-1133 presented at the 11th Fluid and Plasma Dynamics Conference, Seattle, Washington, July 10-12, 1978.

19. Carter, J.E., D. E. Edwards, and M. J. Werle: A New Coordinate Transformation for Turbulent Boundary Layer Flows. Presented at the NASA Workshop on Grid Generation for Partial Differential Equations, held at Langley Research Center, October 6-7, 1980.

20. Chow, R., and R. E. Melnik: Numerical Solutions of the Triple Deck Equations for Laminar Trailing Edge Stall. Proceedings of the Fifth International Conference on Numerical Methods in Fluid Dynamics. Springer Verlag, New York, 1976.

REFERENCES (Cont'd)

21. Jobe, C.E. and O.R. Burggraf: The Numerical Solution of the Asymptotic Equations of Trailing Edge Flow. Proceedings of the Royal Society, London, A 340, pp. 91-111, 1977.

22. Davis, R.T. and Werle, M.J.: Progress on Interacting Boundary Layer Computations at High Reynolds Number. Paper presented at the Conference on Numerical and Physical Aspects of Aerodynamic Flows, California State University, Long Beach, California, January 19-21, 1981.

23. Veldman, A.E.P.: A Numerical Method for the Calculation of Laminar Incompressible Boundary Layers with Strong Viscous-Inviscid Interaction. Report NLR TR 79023, National Aerospace Laboratory, The Netherlands, 1979.

24. Veldman, A.E.P.: A New Calculation of the Wake of a Flat Plate. Journal of Engineering Mathematics, Vol. 9, pp. 65-70, 1975.

25. Veldman, A.E.P.: Boundary Layer Flow Past a Flat Plate. Ph.D. Thesis, Mathematical Institute, University of Groningen, The Netherlands, 1976.

26. Carter, J.E.: Development of a Prediction Method for Transonic Shock Induced Separated Flow. United Technologies Research Center Report R80-915213, prepared under Office of Naval Research Contract N00014-80-C-0424, March 1981.

27. Burggraf, O.R., D. Rizzeta, M. J. Werle, and V. N. Vatsa: Effects of Reynolds Number on Laminar Separation of a Supersonic Stream. AIAA Journal, Vol. 17, No. 4, pp. 336-343, April 1979.

28. Chevray, R. and L.S.G. Kovasznay: Turbulent Measurements in the Wake of a Thin Flat Plate. AIAA Journal, Vol. 7, No. 8, pp. 1641-1643, 1969.

LIST OF SYMBOLS

A	Speed of sound propagation
$A_j, B_j, C_j, D_j, E_{1j}, E_{2j}$	Momentum difference-equation coefficients, Eqs. (71) and (72)
a	Van Driest damping length, Eq. (29b)
$\tilde{a}, \tilde{b}, \tilde{c}, \tilde{d}, \tilde{\gamma}$	Trailing-edge conic-section parameters, Eq. (80c)
C_1, C_2, x_0	Far-wake displacement thickness constants, Eq. (66)
C_L, C_N, C_R	Difference approximation controls, Eq. (73)
C_f	Surface skin friction parameter, Eq. (50)
C_p	Pressure coefficient
c_p	Specific heat at constant pressure
$\mathcal{D}$	Displacement surface
D	Van Driest damping constant, Eq. (29a)
e	Turbulent eddy viscosity
$\tilde{e}$	Normalized viscous parameter, Eq. (72)
$\vec{e}_x$	Unit vector, x-direction
F	Normalized velocity component in shear-layer coordinate direction, Eq. (37)
G	Normalized total enthalpy, Eq. (37)
g	"Turbulent", Levy-Lees, transformation function, Eqs. (35a) and (54)
H	Total enthalpy
H_o	Airfoil height after triple-deck scaling
$h(x)$	Airfoil thickness distribution

LIST OF SYMBOLS (Cont'd)

$h(x)$	Total displacement thickness distribution
$\tilde{h},\tilde{r},R$	Computational coordinate scaling functions, Eq. (70)
h_o	Airfoil height
I_a,I_b,I_c	Integral coefficients, Eq. (60)
K	Mesh scaling parameters, Eqs. (74) and (75)
L	Airfoil length
$\ell,\hat{\ell}$	Levy-Lees viscosity parameters, Eq. (41)
ℓ_{TE}	Length of trailing-edge conic section
M	Mach number
m	Mass flow parameter, Eq. (48)
n	Distance normal to shear-layer coordinate surface
$\tilde{n}$	Scaled normal coordinate, Eq. (18)
$\vec{n}$	Unit normal vector
P	Pressure after triple-deck scaling
P_j,Q_j	Continuity difference-equation parameters, Eq. (69)
p	Pressure
p^+	Pressure gradient in eddy viscosity formula, (Eq. 29c)
q	Heat transfer rate, Eq. (25)
$\vec{R}$	Position vector, Eq. (4)
r	Distance ratio, Eq. (76)
Re	Reynolds number

LIST OF SYMBOLS (Cont'd)

$\mathcal{S}$	Shear-layer coordinate surface
S,N	Computational coordinates
s	Distance along shear-layer coordinate surface
s_{ti}	Location of transition initiation, Eq. (31a)
T	Temperature
t(s)	Function which defines location of airfoil surface, Eq. (5)
$U_{\mathcal{L}}$	Wake-centerline velocity
u	Velocity component in shear-layer coordinate direction
u_{calc}	Wake velocity profile, Eq. (30b)
u_τ	Shear velocity, Eq. (29d)
V	Levy-Lees dependent variable, Eq. (37)
v	Normal velocity component
$\tilde{v}$	Scaled normal velocity component, Eq. (18)
X,Y	Distances along and normal to airfoil chord after triple-deck scaling.
x	Distance along airfoil chord
y	Distance normal to airfoil chord
α	Levy-Lees parameter, Eqs. (41) and (47a)
α_w, α_f	Trailing-edge angles, Fig. 5a
β	Levy-Lees pressure gradient parameter, Eqs. (41) and (47b)
$\tilde{\gamma}$	Scaled pressure gradient, Eq. (72)

LIST OF SYMBOLS (Cont'd)

γ	Specific heat ratio
γ_T	Longitudinal intermittency factor, Eq. (31a)
δ	Viscous displacement thickness
ε	Small parameter, Eqs. (6) and (33)
η	Levy-Lees normal coordinate, Eq. (35b)
θ	Density integral, Eq. (52)
λ_T	Scale length of transition process, Eq. (31b)
μ	Viscosity
$\mu_T, \hat{\mu}_T$	Effective turbulent viscosities, Eq. (22)
ξ	Levy-Lees streamwise coordinate, Eq. (35a)
ρ	Density
σ	Prandtl number
σ_T	Turbulent Prandtl number
$\vec{t}$	Unit vector tangent to shear-layer coordinate surface, Eq. (11)
Φ	Velocity potential
ϕ	First-order velocity potential, Eq. (6)
$\tilde{\phi}$	Coordinate surface inclination angle, Eq. (79)
ω	relaxation parameter, Eq. (32)

Superscripts

n	nth iterative estimate
'	Differentiation

LIST OF SYMBOLS (Cont'd)

Superscripts

*	Dimensional quantity

Subcripts

$\mathcal{D}$	Displacement surface
d	Downstream
e	Edge of viscous layer
i	Inner region of turbulent layer, grid point index in shear-layer coordinate direction
inv	Inviscid solution
j	Grid point index
o	Outer region of turbulent layer
max	Maximum value
$\mathcal{S}$	Shear-layer coordinate surface
T	Turbulence parameter
TE	Trailing edge
u	Upstream
visc	Viscous solution
W	Wall
w	Inner region of turbulent wake
0	Zeroth-order perturbation quantity, Eq. (6), previous station in viscous layer computation

LIST OF SYMBOLS (Cont'd)

Subscripts

1	First-order perturbation quantity, upstream boundary of computational region
∞	Free-stream conditions
I,II	Systems of linear algebraic equations, Eq. (57)

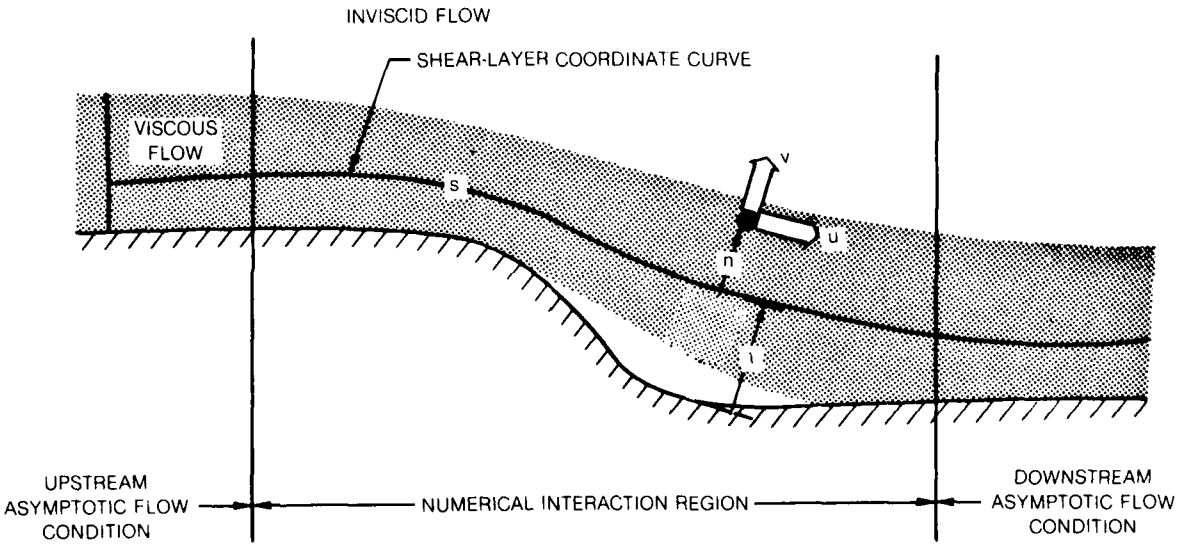

Figure 1 Flow Field Nomenclature

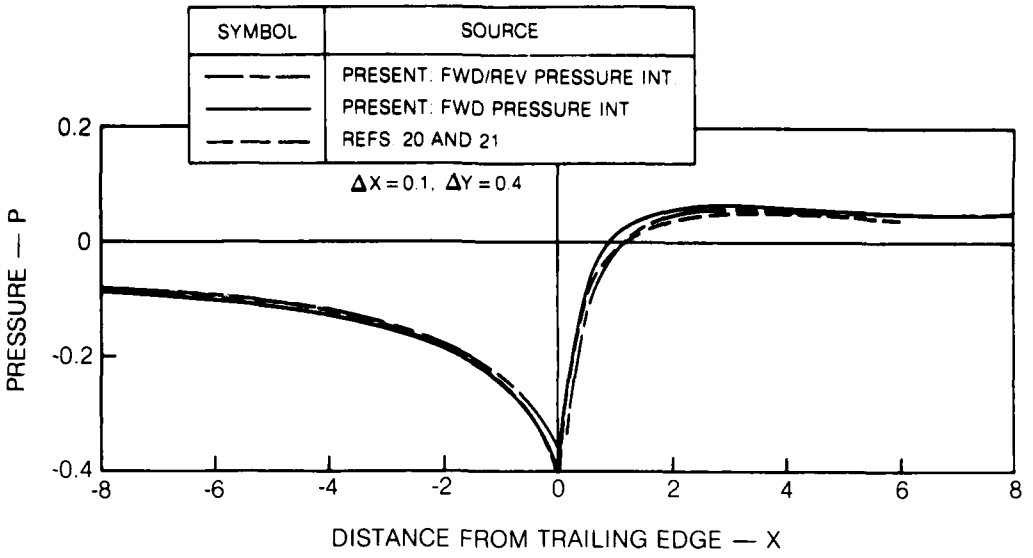

Figure 2 Flat-Plate Triple-Deck Pressure Distributions
(a) Overall Solution

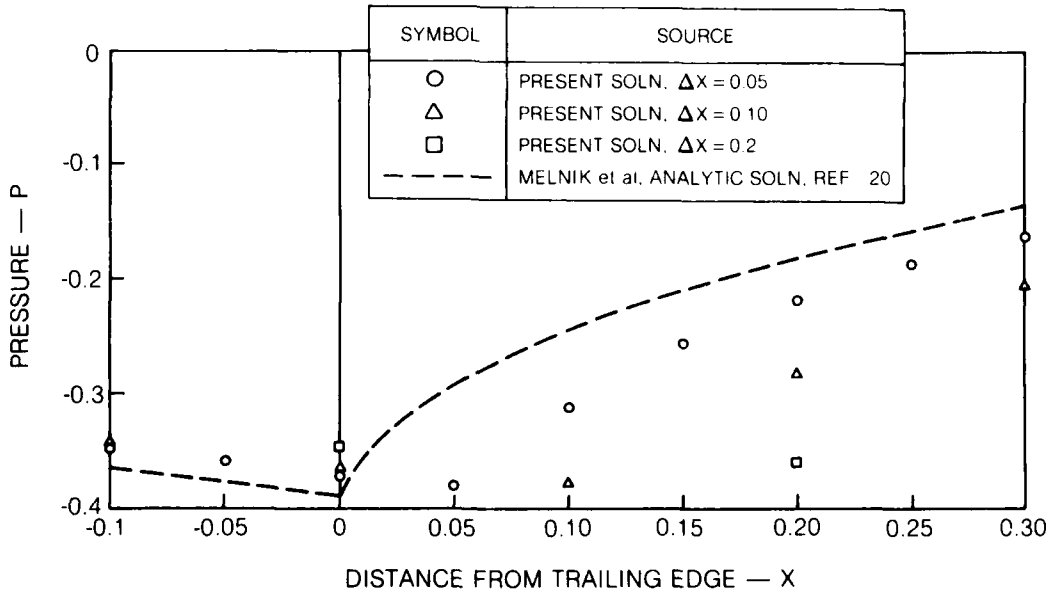

Figure 2 Flat-Plate Triple-Deck Pressure Distributions
(b) Trailing Edge Region

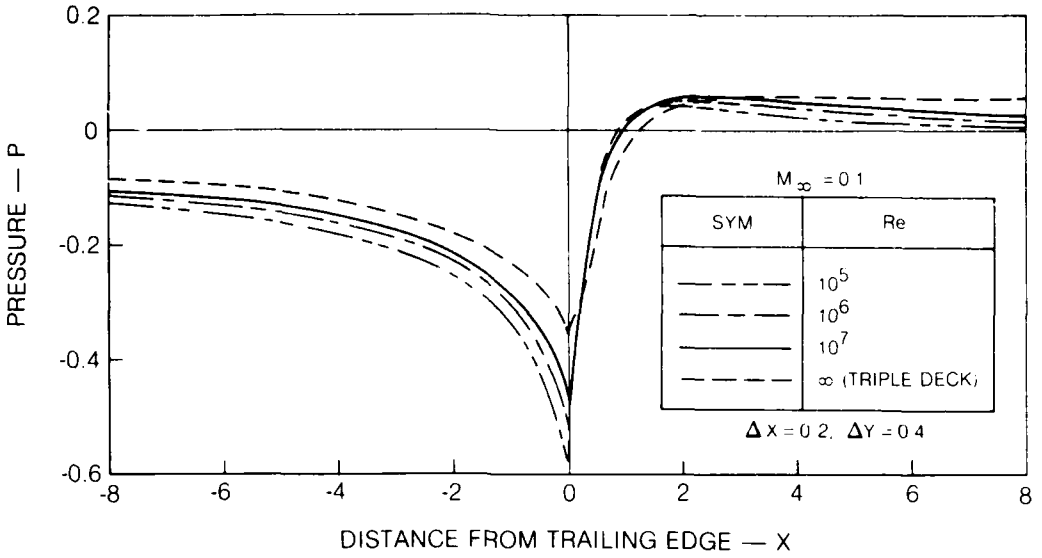

Figure 3 Flat-Plate Interacting Boundary Layer Solutions
(a) Reynolds Number Effect — Forward/Reverse Integration

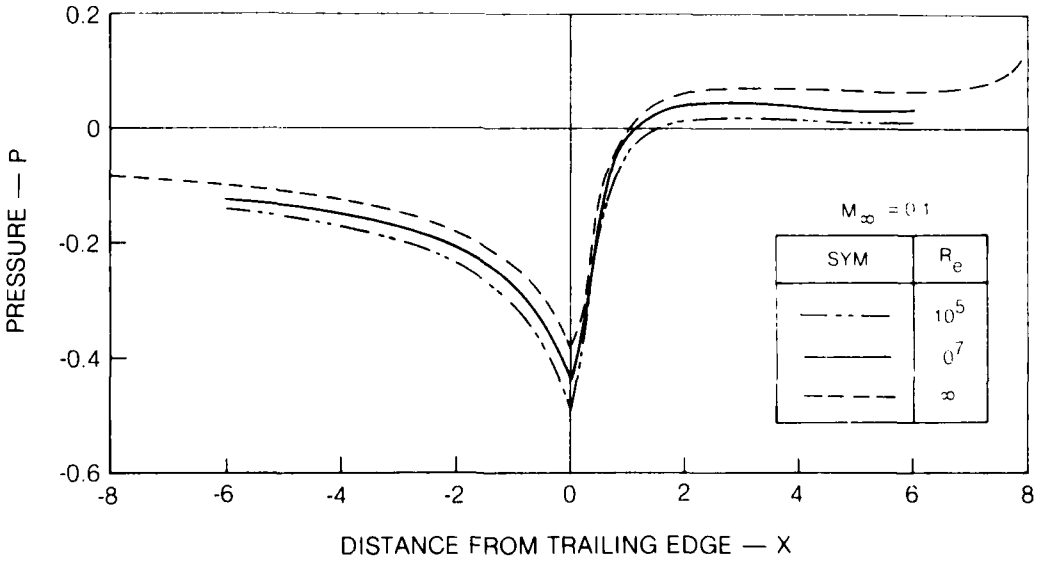

Figure 3 Flat-Plate Interacting Boundary Layer Solutions
(b) Reynolds Number Effect — Forward Integration

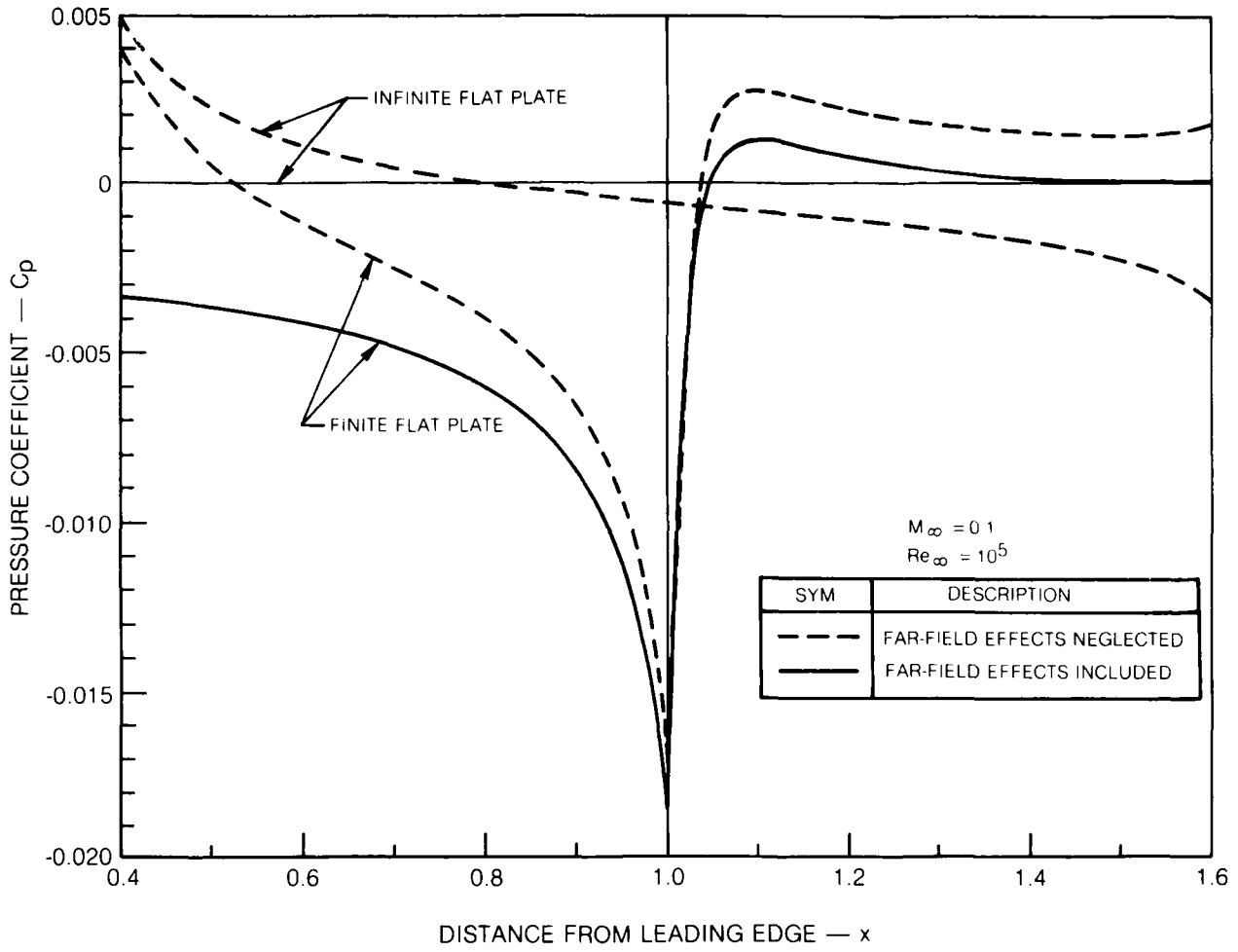

Figure 3 Flat-Plate Interacting Boundary Layer Solutions
(c) Global Interaction Effects

80-10-165-33

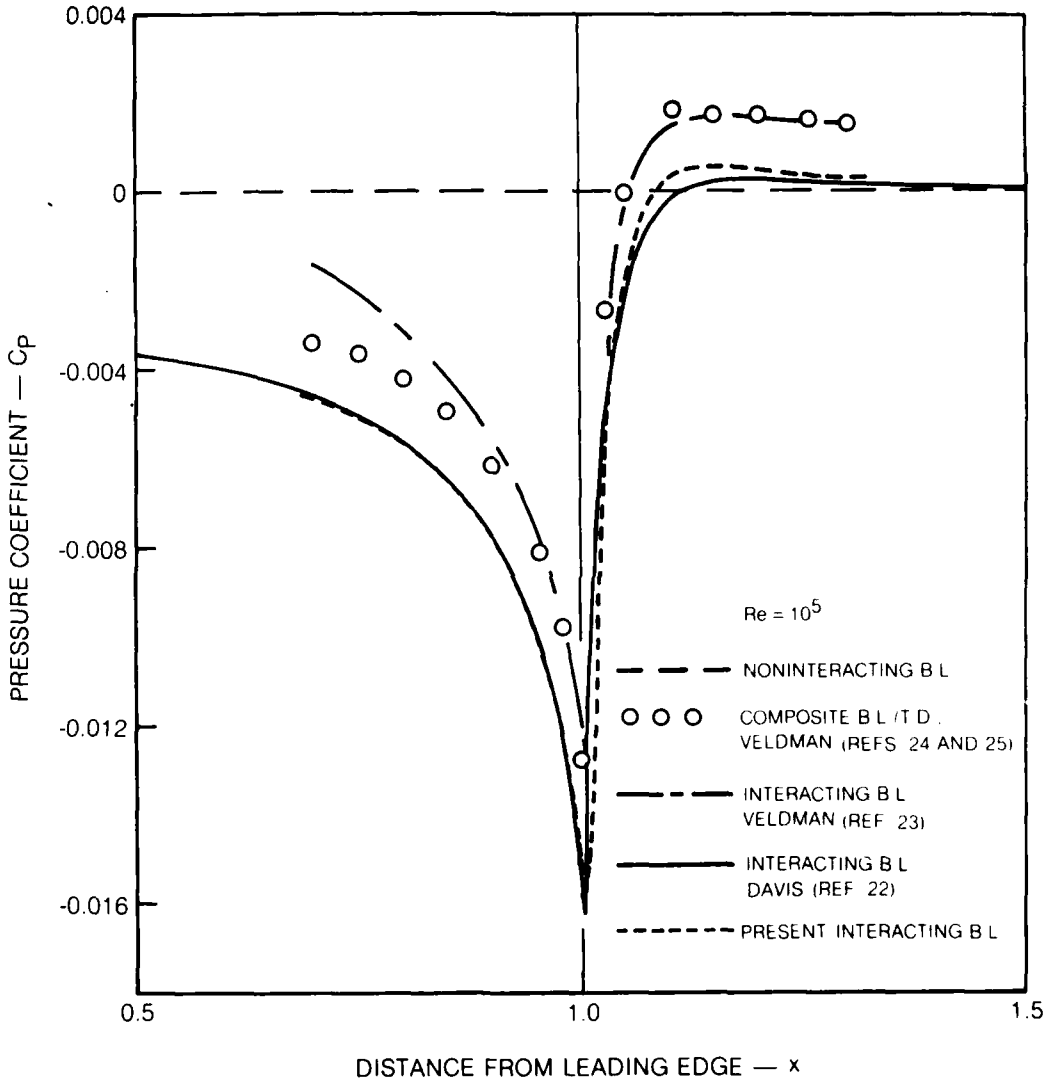

Figure 4 Finite Reynolds Number Solutions for a Flat-Plate Trailing Edge (a) Surface Pressure

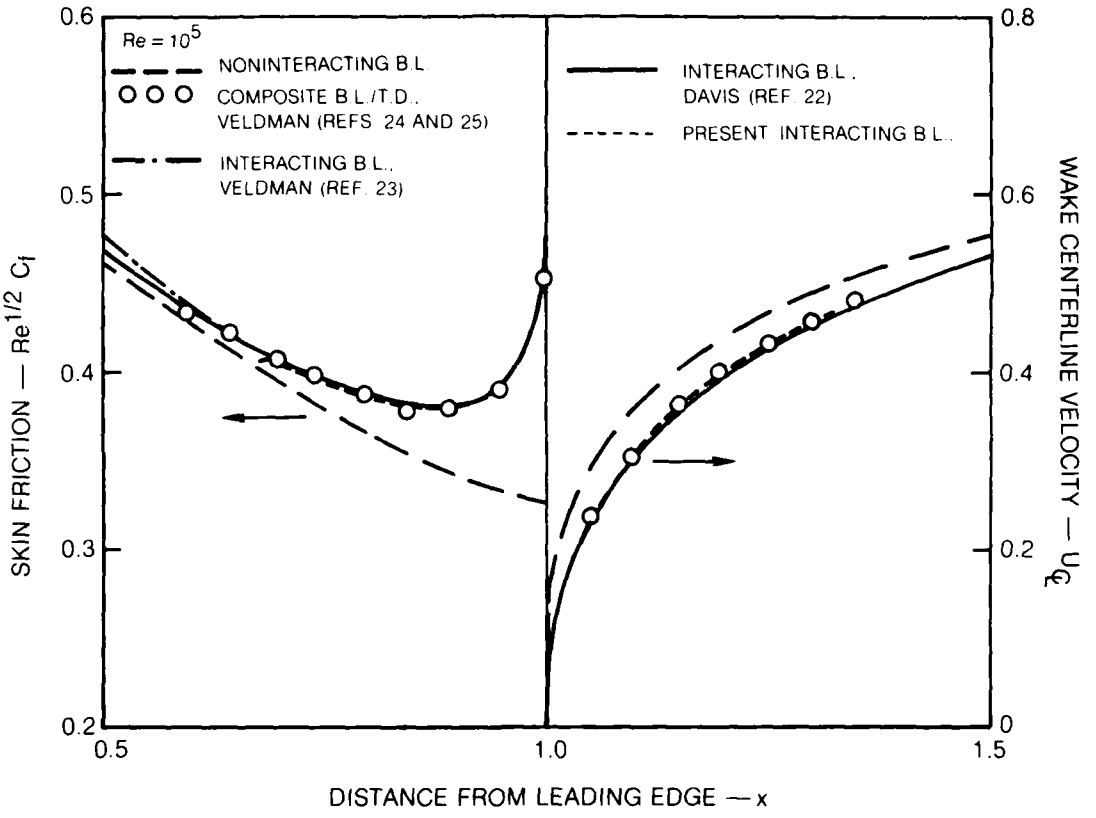

Figure 4 Finite Reynolds Number Solutions for a Flat-Plate Trailing Edge (b) Skin Friction and Wake Centerline Velocity

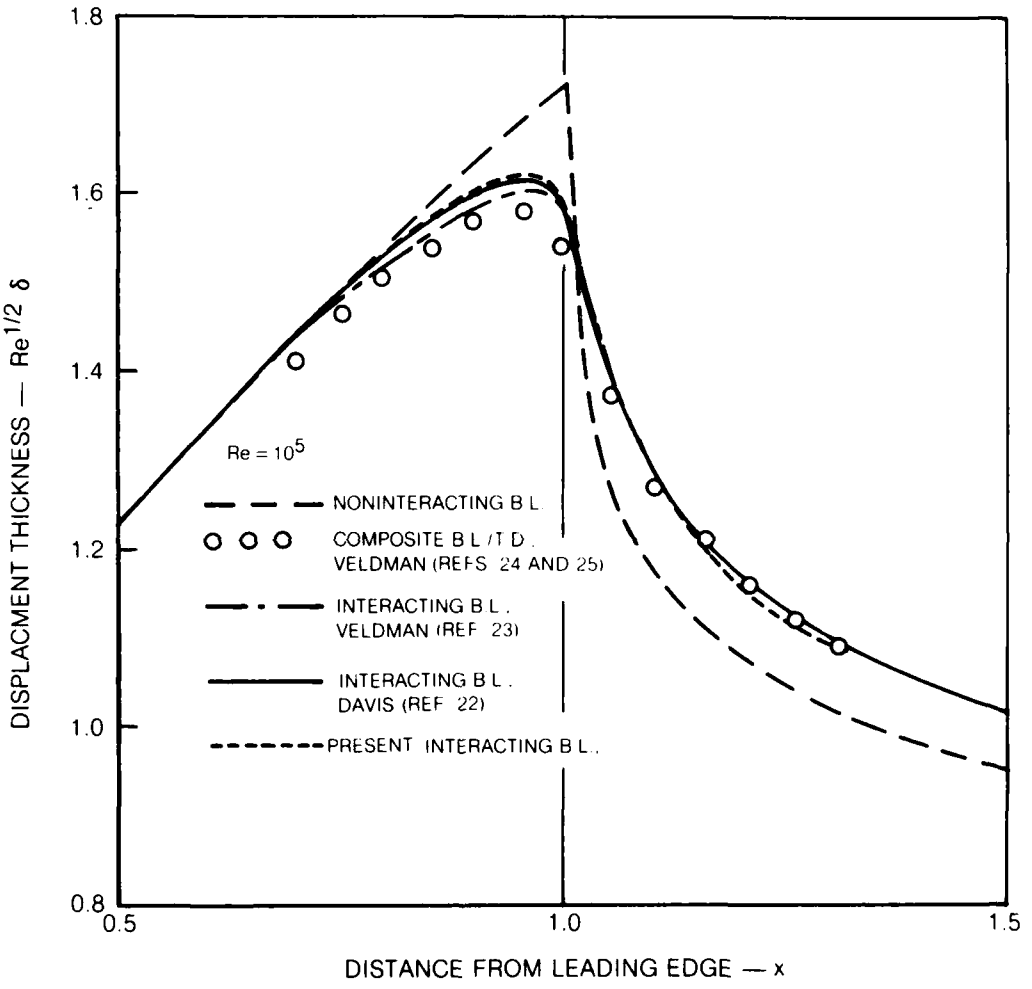

Figure 4 Finite Reynolds Number Solutions for a Flat-Plate Trailing Edge (c) Displacement Thickness

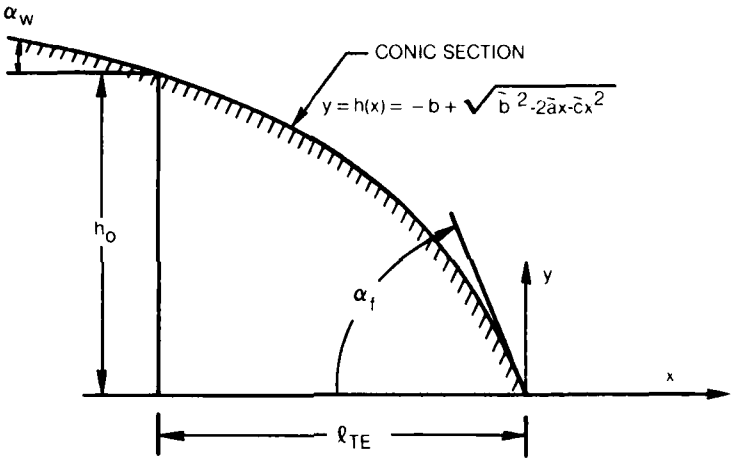

Figure 5 Laminar Blunt Trailing Edge Solutions
(a) Trailing Edge Geometry

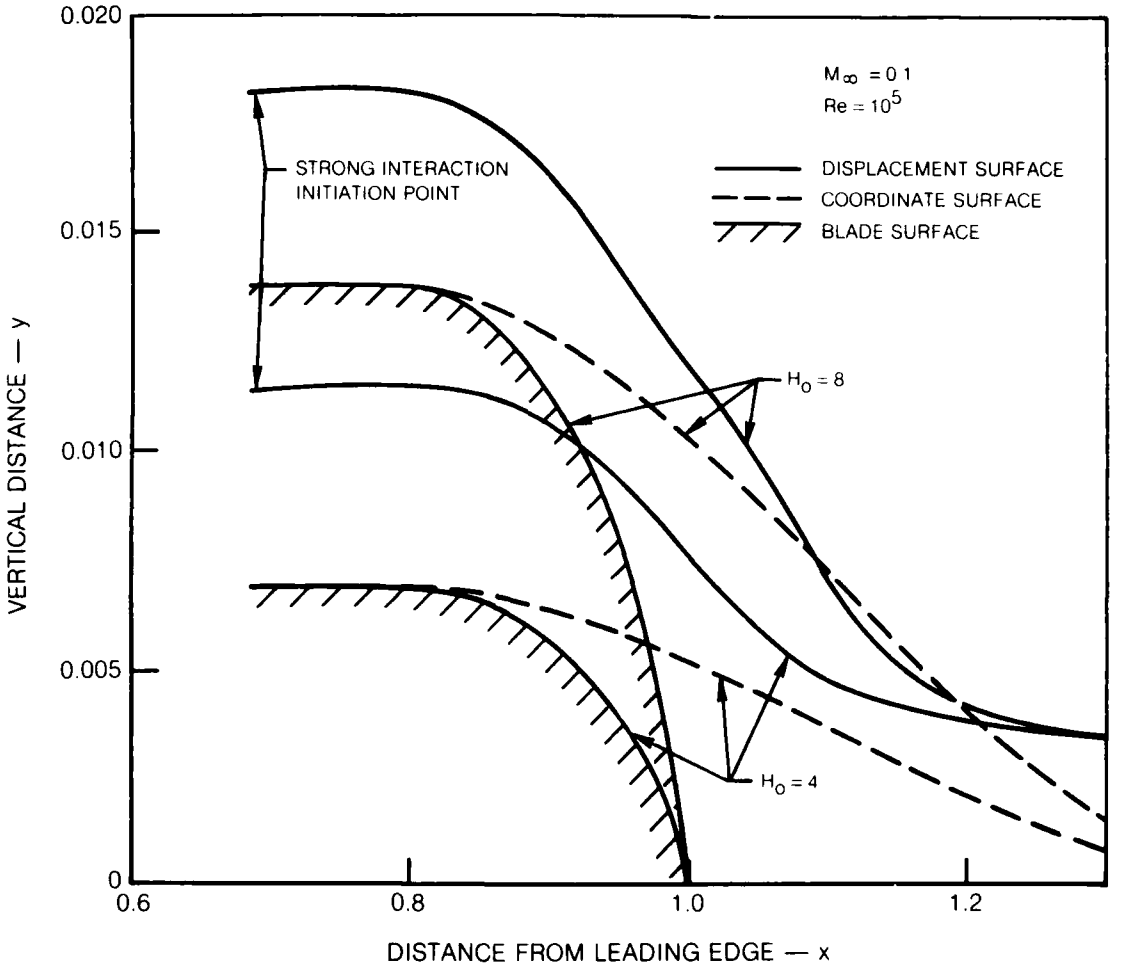

Figure 5 Laminar Blunt Trailing Edge Solutions
(b) Displacement Surface

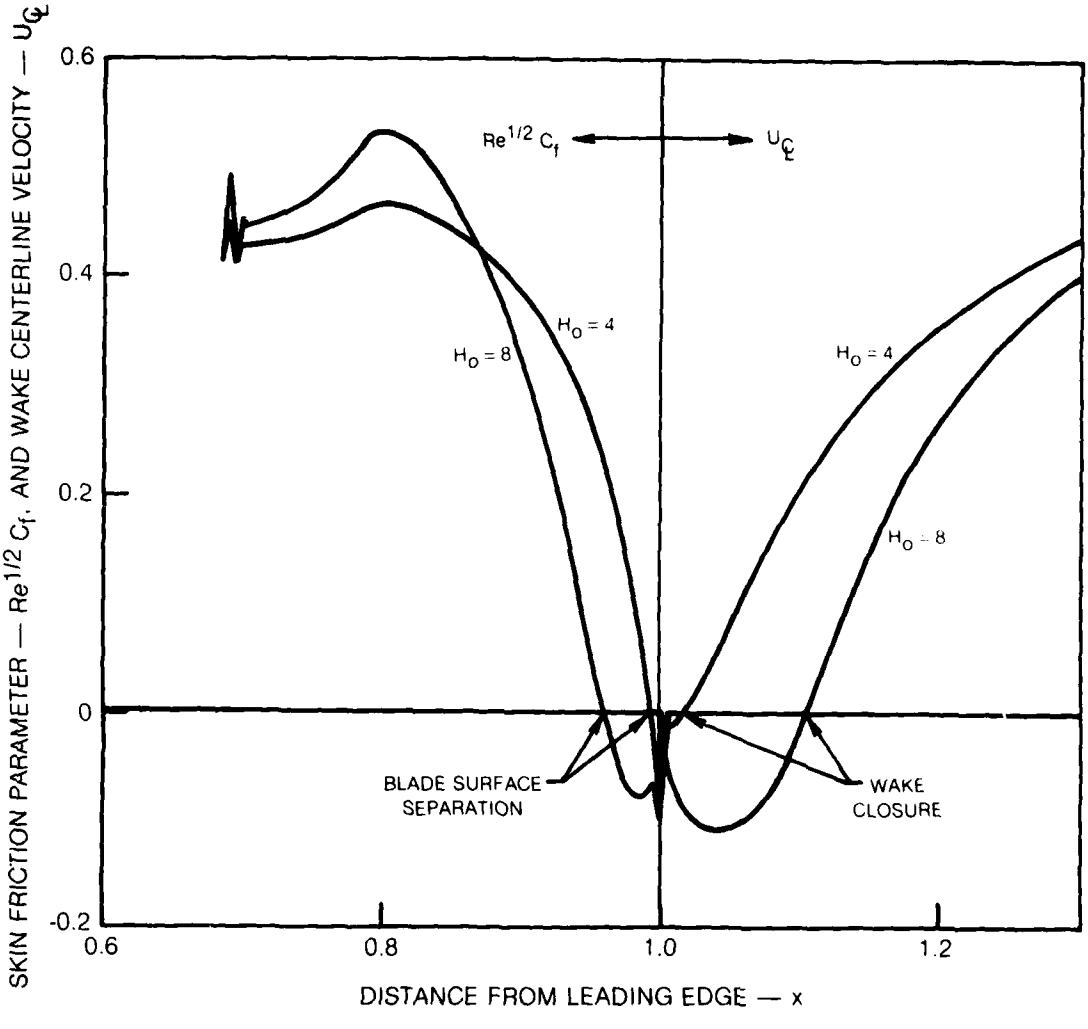

Figure 5 Laminar Blunt Trailing Edge Solutions
(c) Skin Friction Parameter and Wake Centerline Velocity

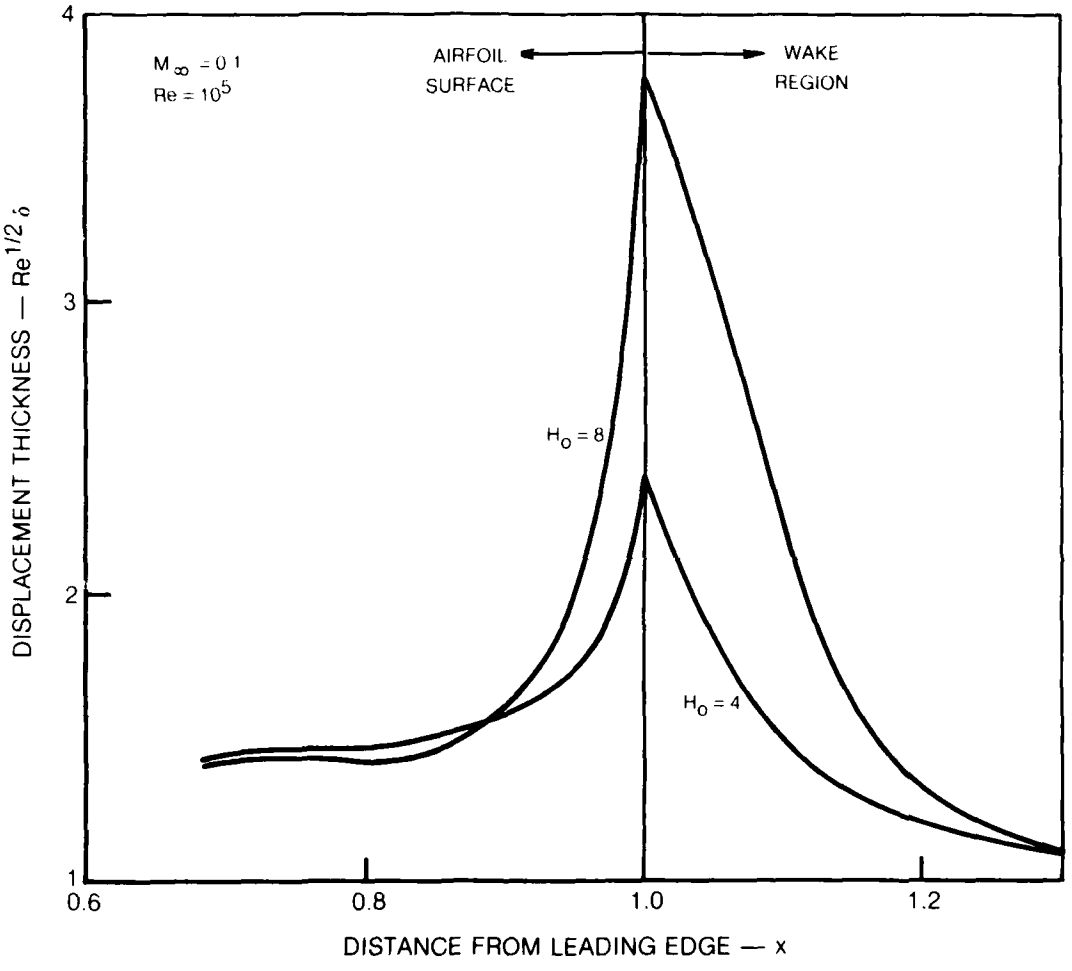

Figure 5 Laminar Blunt Trailing Edge Solutions
(d) Displacement Thickness

80-10-165-23

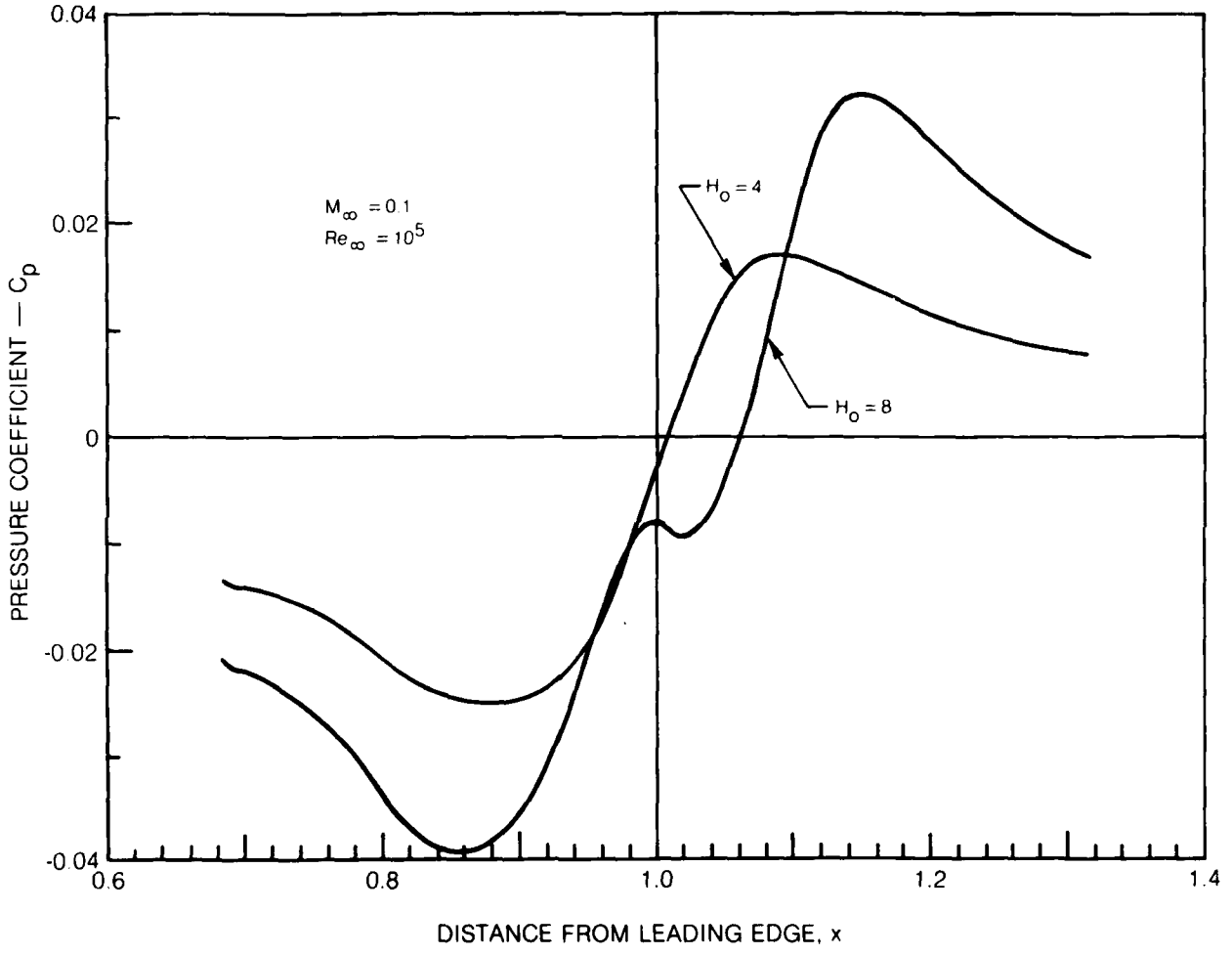

Figure 5 Laminar Blunt Trailing Edge Solutions
(e) Pressure Distribution

80-10-165-32

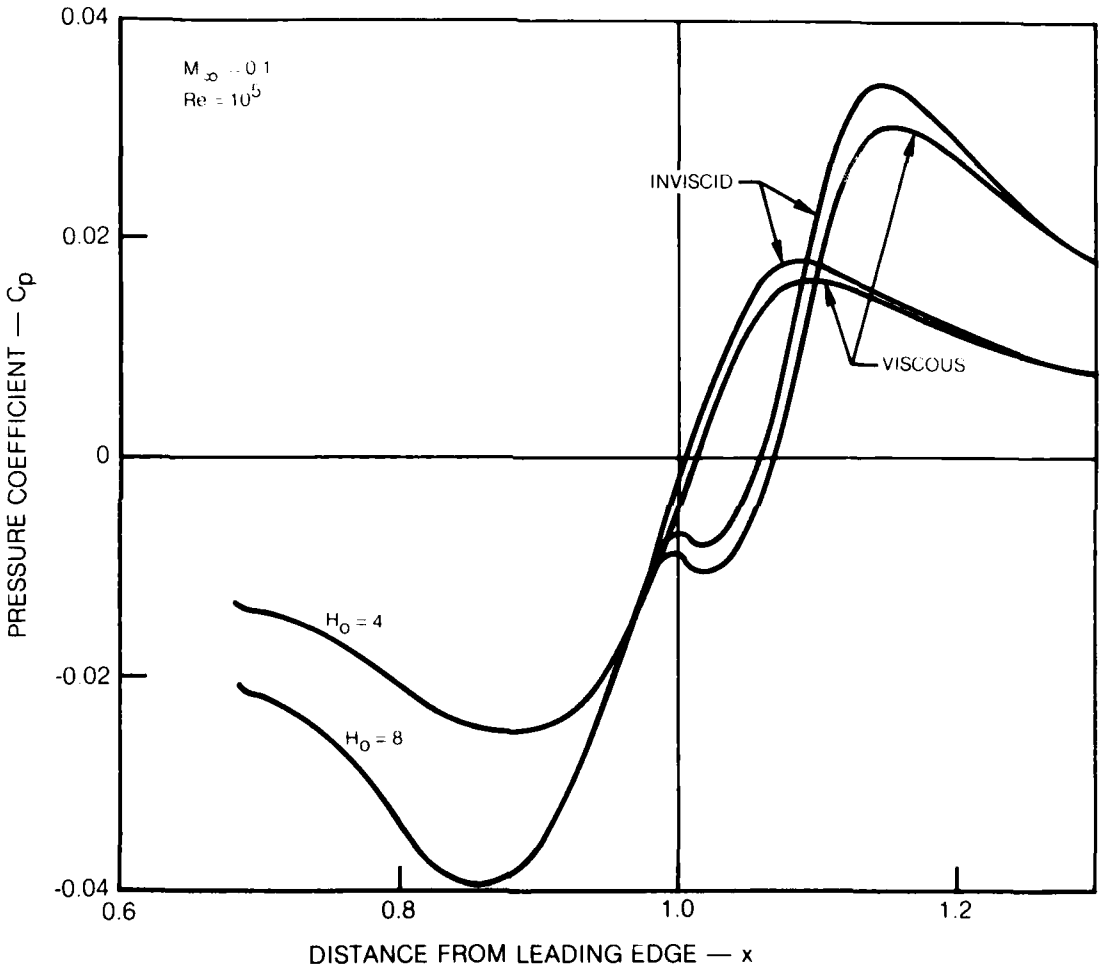

Figure 5 Laminar Blunt Trailing Edge Solutions
(f) Viscous and Inviscid Pressure Levels

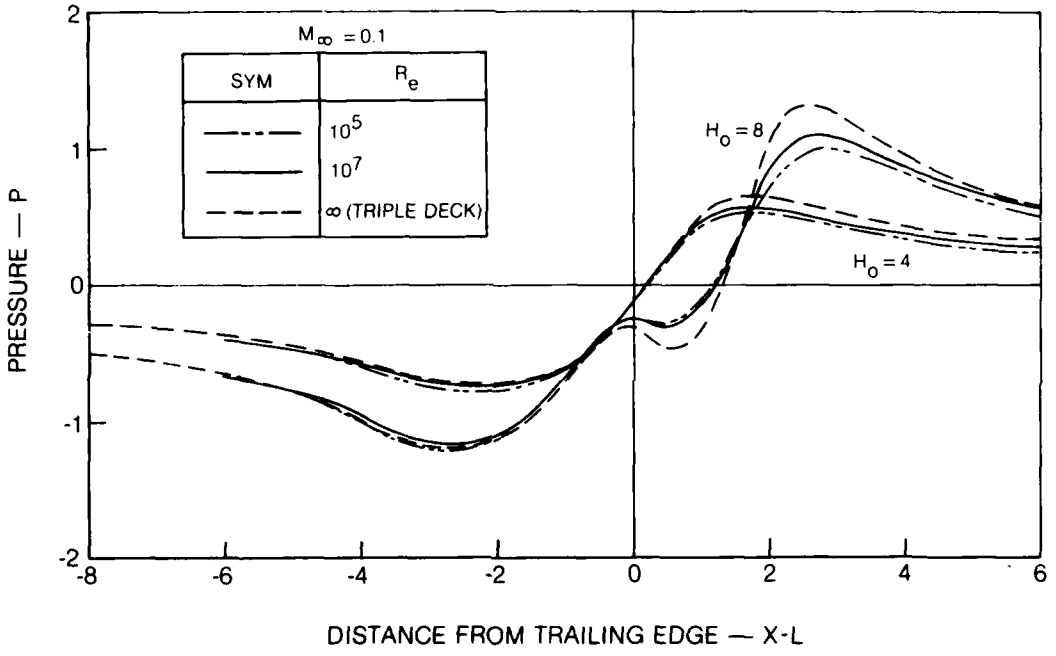

Figure 6 Reynolds Number Effects for Laminar Blunt Trailing Edges (a) Surface Pressure

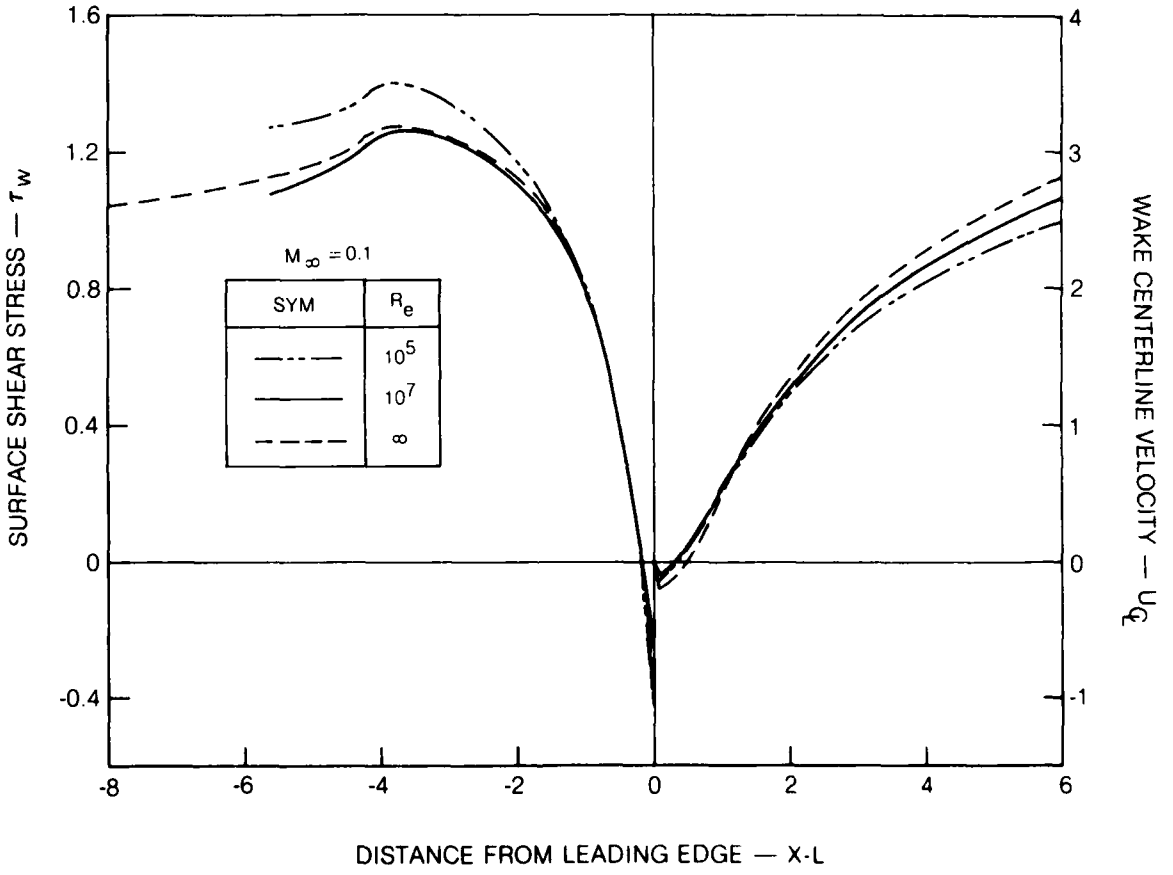

Figure 6 Reynolds Number Effects for Laminar Blunt Trailing Edges
(b) Surface Shear Stress and Wake Centerline Velocity — $H_o = 4$

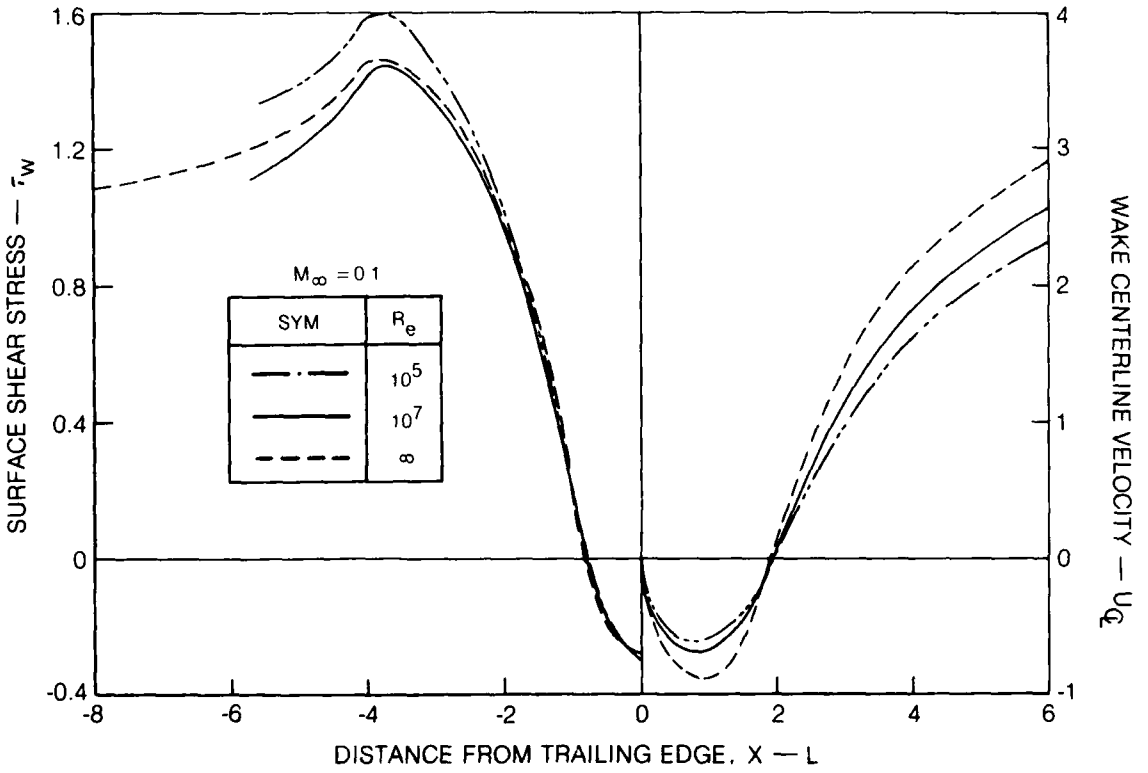

Figure 6 Reynolds Number Effects for Laminar Blunt Trailing Edges (c) Surface Shear Stress and Wake Centerline Velocity — $H_o = 8$

81-1-88-2

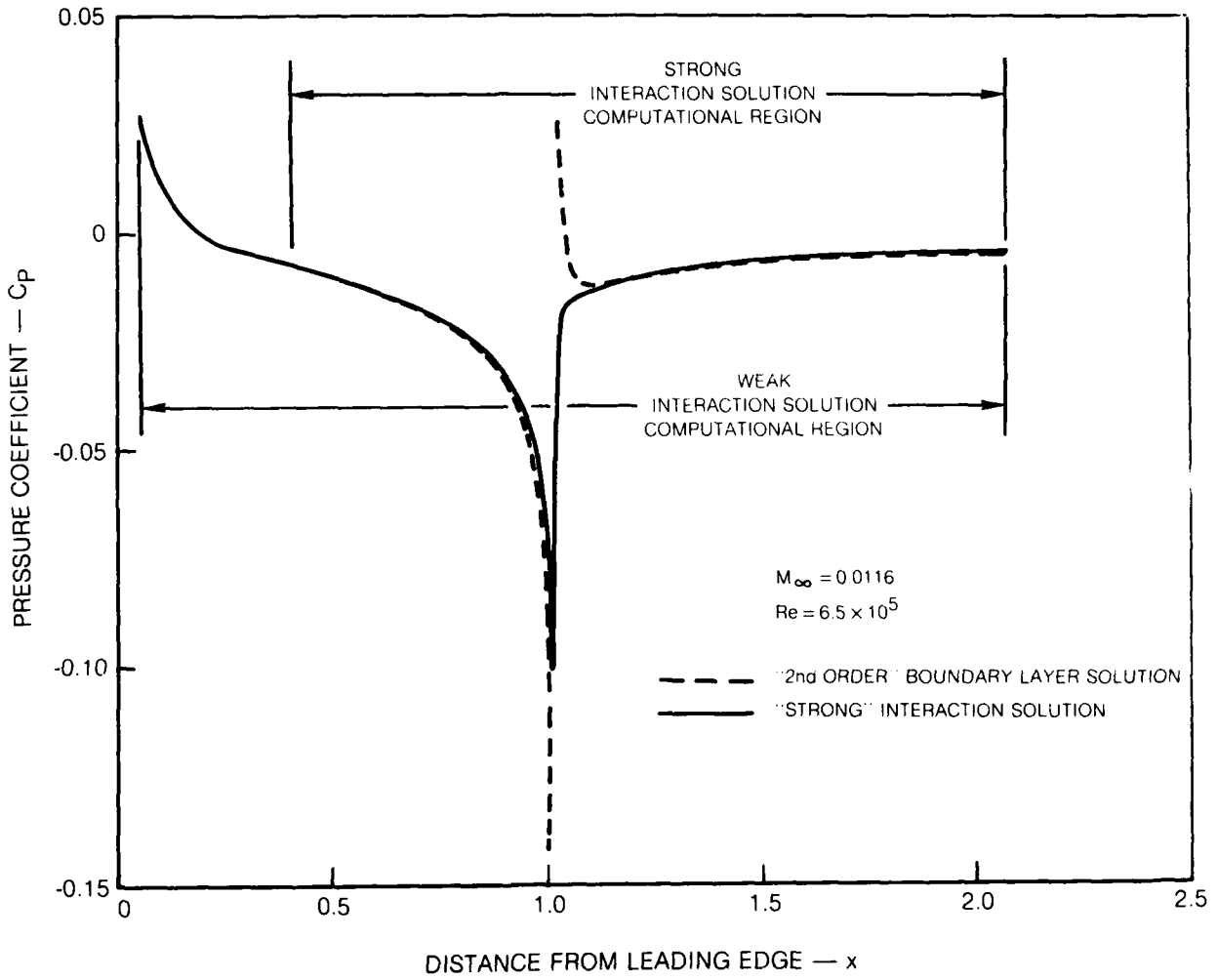

Figure 7 Turbulent Flat Plate Results
(a) Pressure Coefficient

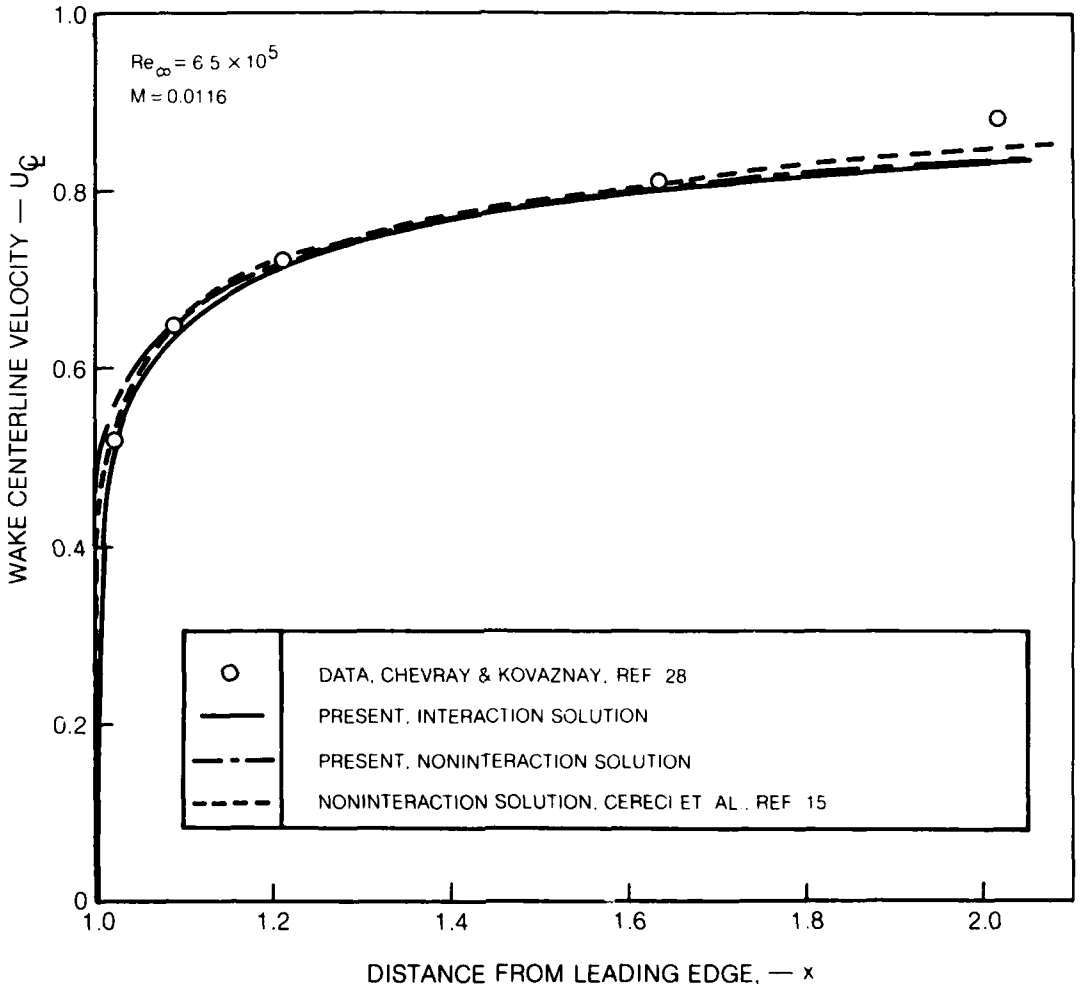

Figure 7 Turbulent Flat Plate Results
(b) Wake Centerline Velocity

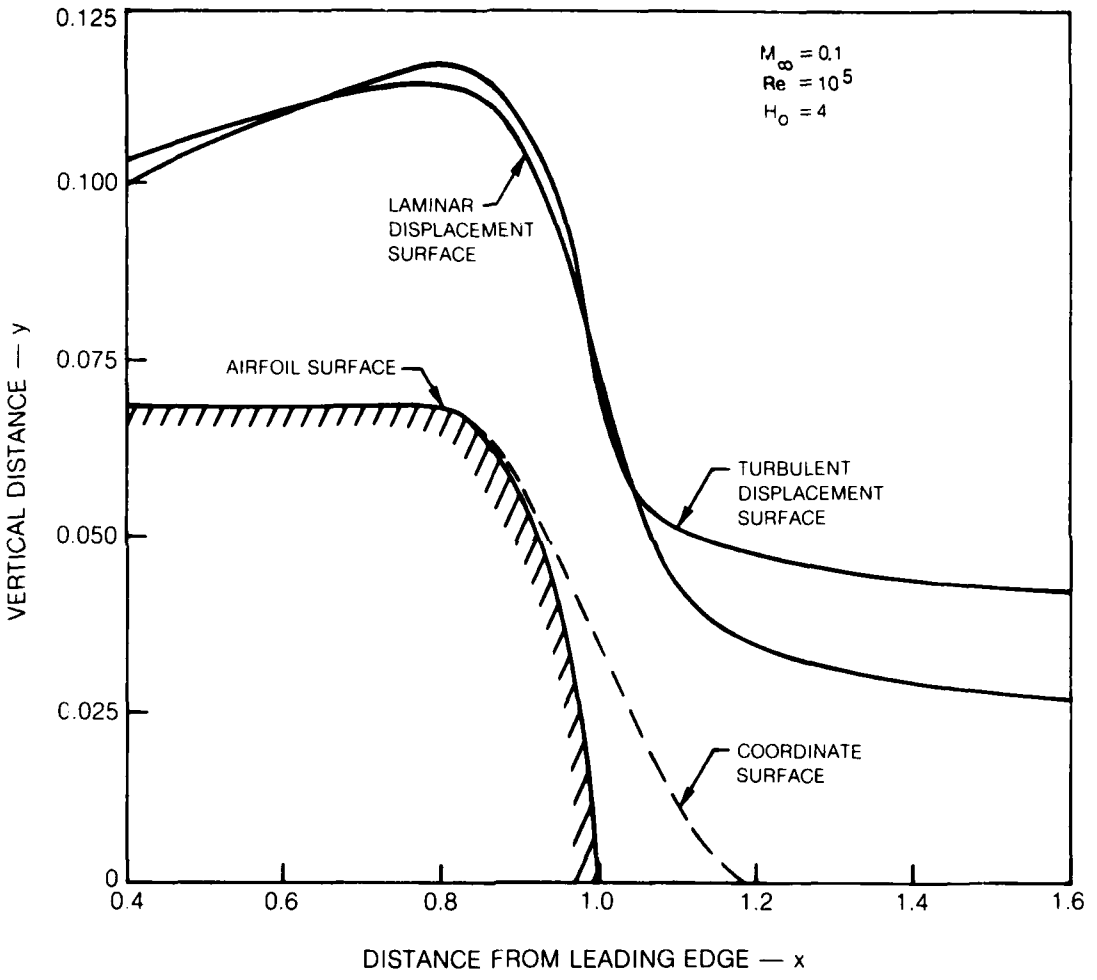

Figure 8 Turbulent Blunt Trailing Edge Solutions
(a) Displacement Surface

80-10-165-28

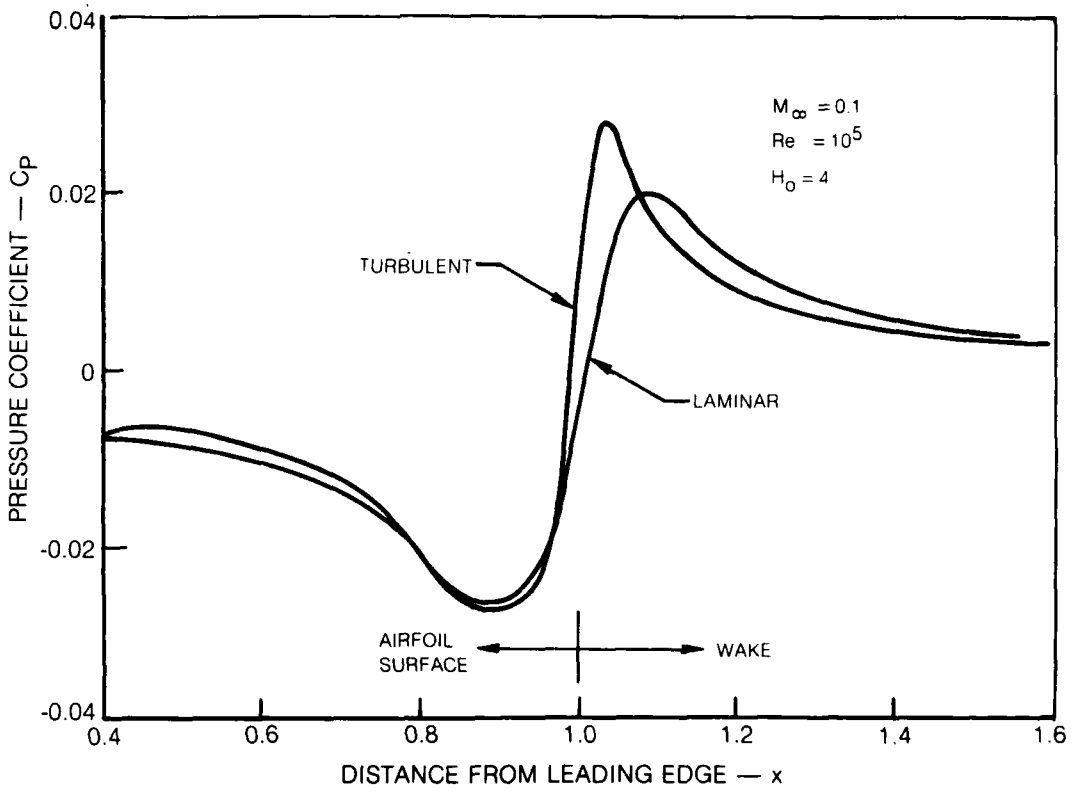

Figure 8 Turbulent Blunt Trailing Edge Solutions
(b) Pressure Coefficient

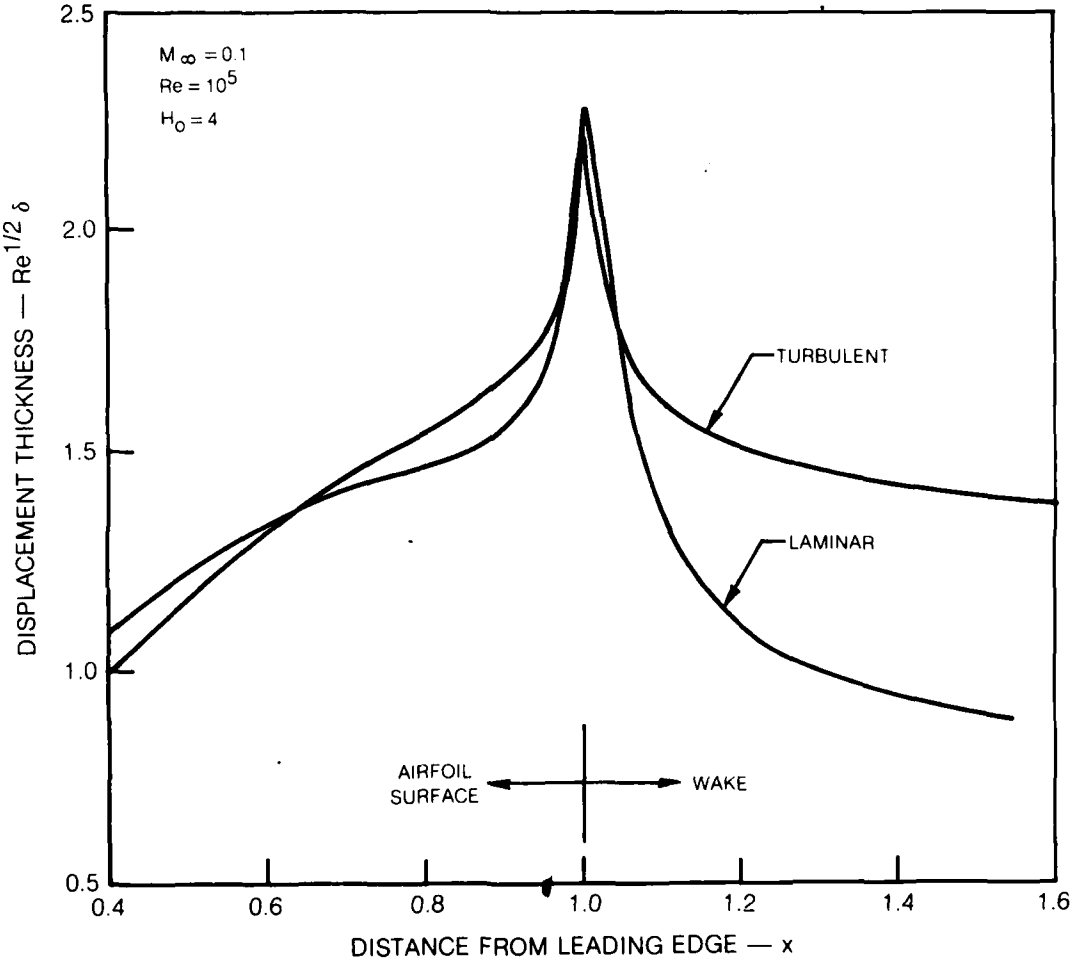

Figure 8 Turbulent Blunt Trailing Edge Solution
(c) Displacement Thickness

80-10-165-20

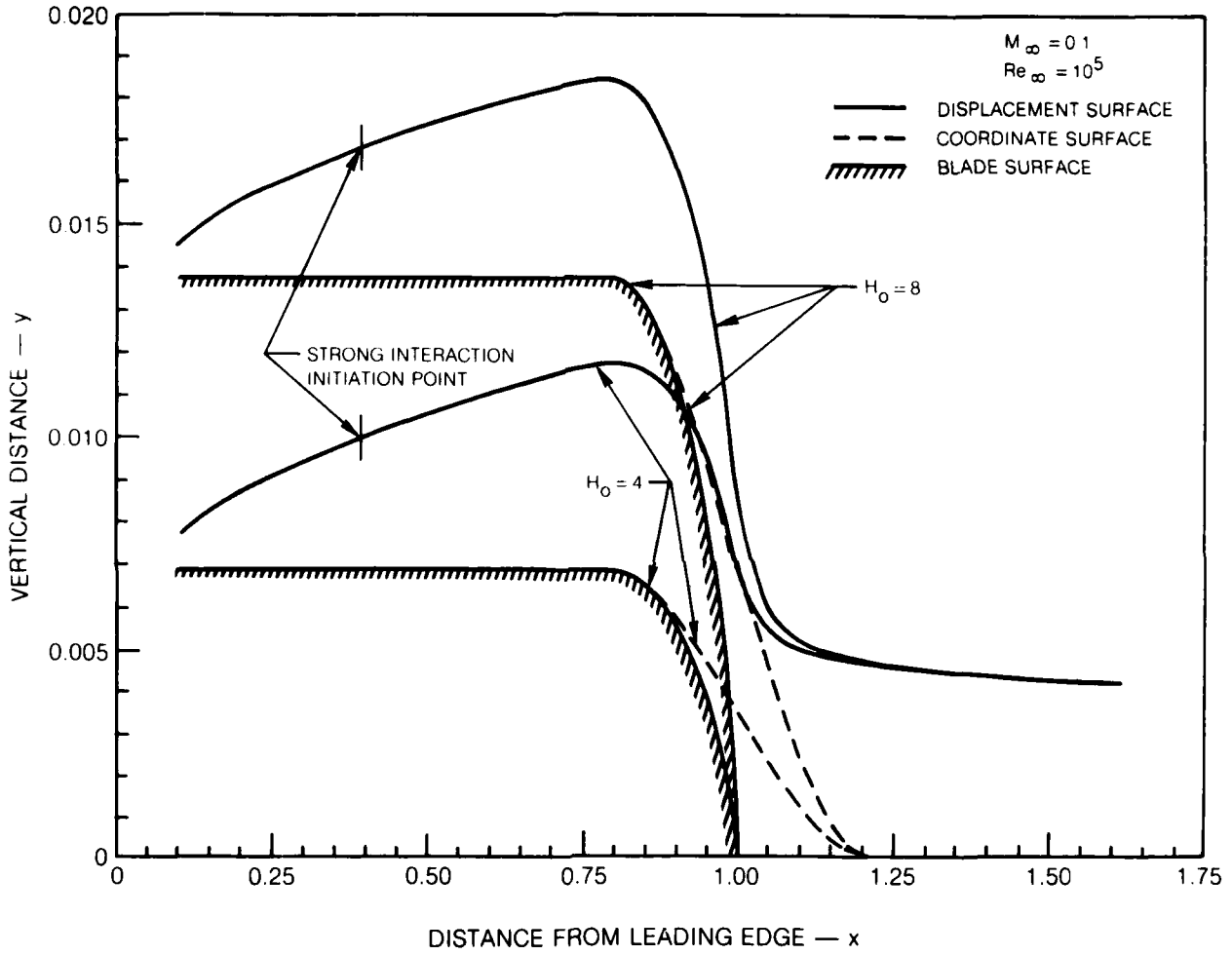

Figure 9 Effect of Airfoil Thickness on Turbulent Trailing Edge Flow
(a) Displacement Surface

80-10-165-31

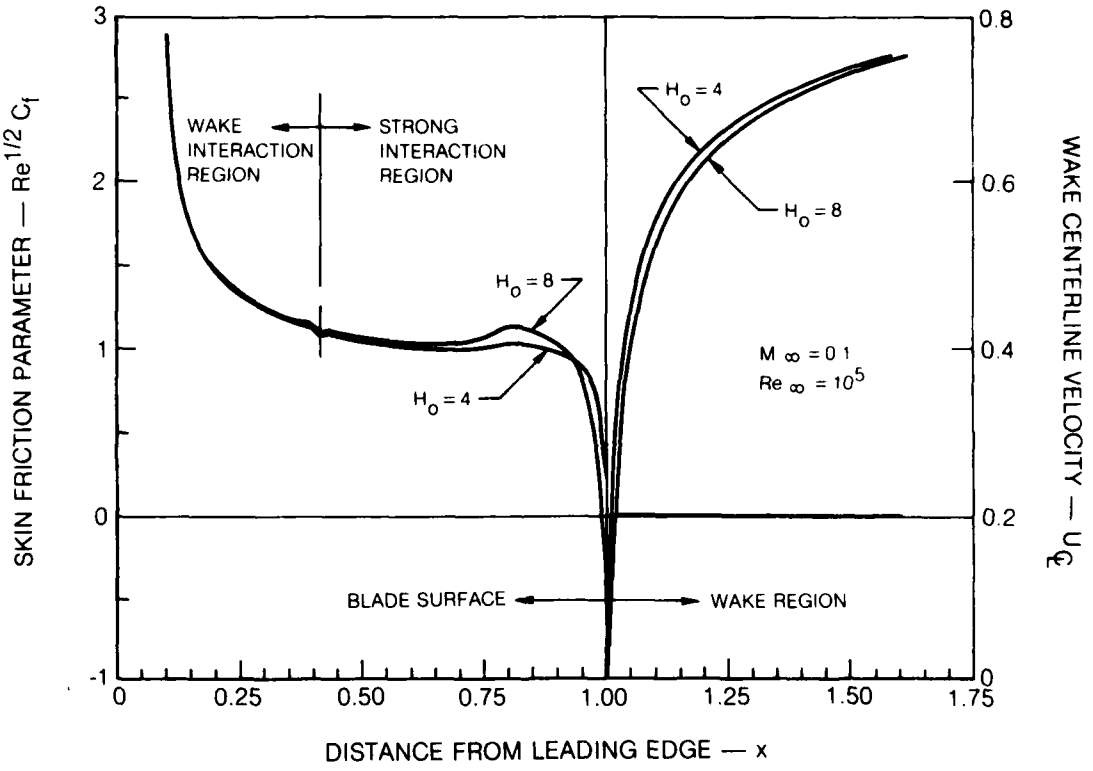

Figure 9 Effect of Airfoil Thickness on Turbulent Trailing Edge Flow (b) Skin Friction Parameter and Wake Centerline Velocity

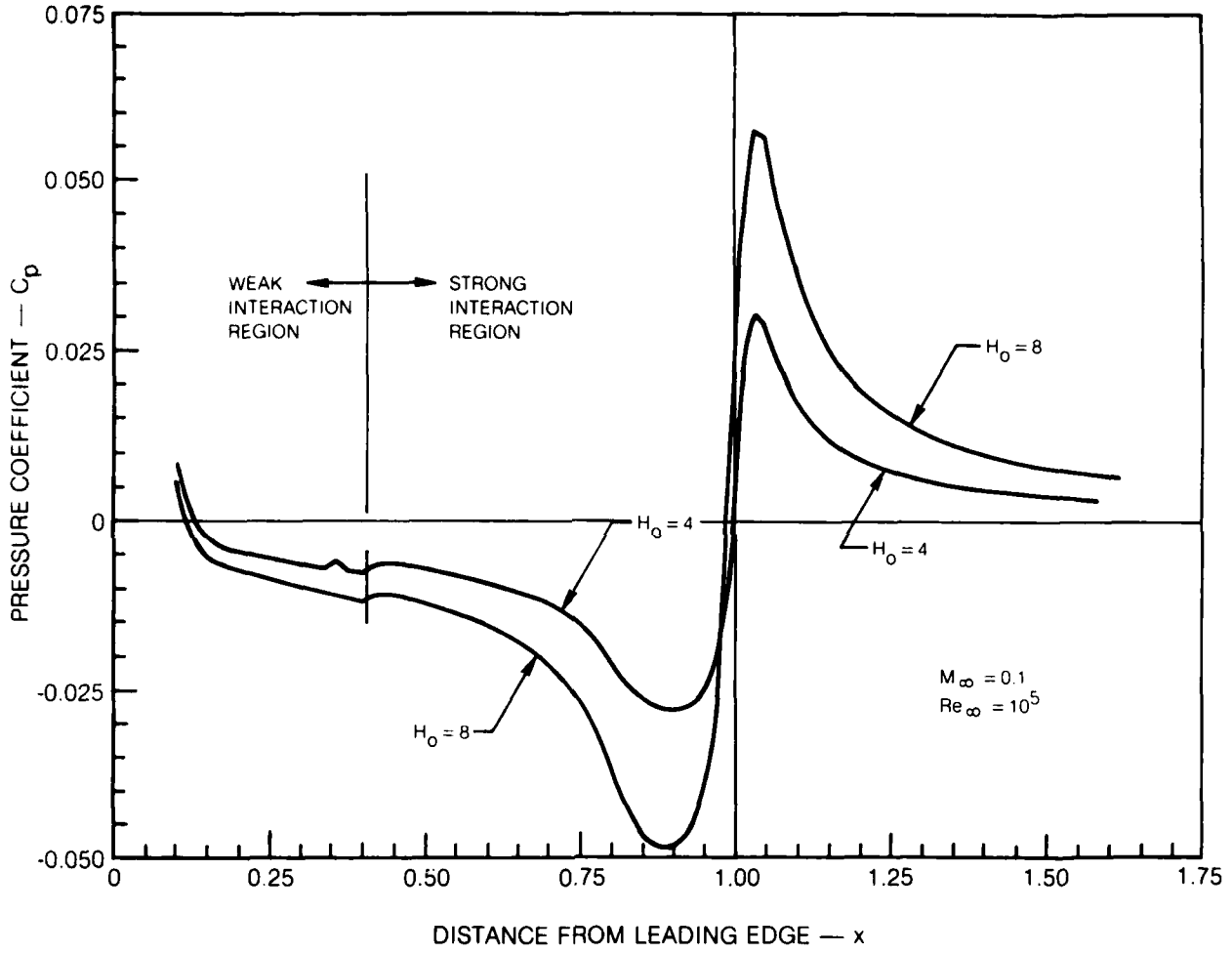

Figure 9 Effect of Airfoil Thickness on Turbulent Trailing Edge Flow (c) Pressure Coefficient

80-10-165-29